On the best design for undulatory swimming

Christophe Eloy[1,2]†

[1]Aix–Marseille University, IRPHE UMR 7342, CNRS, 13013 Marseille, France

[2]Department of Mechanical and Aerospace Engineering, University of California San Diego, La Jolla, California 92093, USA

Most aquatic vertebrates swim by passing a bending wave down their bodies, a swimming mode known as undulatory propulsion. Except for very elongated swimmers like eels and lampreys, these animals have evolved to a similar shape: an anterior streamlined region of large volume separated from a caudal fin by a caudal peduncle of reduced cross-section. However, the link between this particular shape and the hydrodynamical constraints remains to be explored. Here, this question is addressed by seeking the optimal design for undulatory swimmers with an evolutionary algorithm. Animals of varying elliptic cross-section are considered whose motions are prescribed by arbitrary periodic curvature laws. In the elongated-body limit, reactive and resistive forces can be formulated at any cross-section, allowing to calculate the recoil motion and the mean swimming speed of a given animal. A bi-objective optimisation problem then consists in finding body shapes and corresponding motions associated with the highest swimming velocities, the lowest energetic costs, or any trade-offs between the two. For biologically relevant parameters, this optimisation calculation yields two distinct 'species': one specialised in economical swimming and the other in fast swimming. By comparing, the attributes and performances of these numerically-obtained swimmers with data on undulatory-swimming animals, it is argued that evolution is consistent with low energetic costs.

1. Introduction

There are presumably more than 30,000 different species of fish, the majority of them using 'undulatory swimming' as their main mode of locomotion. This mode is sometimes also called 'body and caudal fin' propulsion, and is different from 'median and paired fin' propulsion in that animals use the bending of their backbones to achieve locomotion (Blake 2004). The kinematics and performances of undulatory swimmers have been widely studied in the literature, starting with the pioneering works of Gray (1933) and Bainbridge (1958, 1963), and have been reviewed numerous times (e.g. Gray 1968; Lighthill 1969; Alexander 1977; Blake 1983; Fish & Hui 1991; Videler 1993; Triantafyllou *et al.* 2000; Lauder & Tytell 2005; Wu 2011).

Observing their designs, one can distinguish two groups of undulatory swimmers: elongated eel-like swimmers, and salmon-like or tuna-like ones. The elongated swimmers have aspect ratios of the order of 10 or more and their cross-section generally varies moderately along their length. Their swimming gaits involve the bending of their whole body with an envelope that grows almost linearly from head to tail. Salmon-like or tuna-like swimmers have been divided into three subclasses (sub-carangiform, carangiform, and thunniform swimmers) by Lindsey (1978) according to the localisation of their bending along the backbone, but these subdivisions are not related to any phylogenetic considerations, and describe a continuum of shapes and motions that share common characteristics (Blake

† Email address for correspondence: eloy@irphe.univ-mrs.fr

2004; Lauder & Tytell 2005). These salmon-like swimmers have usually an aspect ratio of the order of 5, with a large and streamlined anterior region that accounts for most of the animal mass. This anterior region is separated from a caudal fin of similar height by the caudal peduncle, which is generally of markedly reduced cross-section. As eel-like swimmers, the salmon-like swimmers generate thrust by propagating a bending wave down to their caudal fin, but large curvatures are now localised in the posterior region (again, the extent of this localisation leads to the subclasses defined by Lindsey 1978).

To use a vocabulary common in evolutionary biology, these two classes of undulatory swimmers (the eel-like group and the salmon-like group) likely correspond to local peaks of the fitness landscape. Examples of convergent evolution give other evidence of the attractive nature of these two groups, canonical examples being the convergent evolution of sharks, dolphins, and reptilian ichthyosaurs (species now extinct 90 My ago), which belong to the salmon-like group (Lighthill 1969), or the convergent evolution of eels and lampreys that are different from a phylogenetic viewpoint but belong to the eel-like group. It seems reasonable to assume that evolution selected these two groups of undulatory swimmers because of their superior swimming performances over all possible shapes and motions. However, it is still unclear which of the performances have served as selective pressures. Or, said differently, the design principles behind undulatory swimming are still largely unknown. Addressing this open question with biological and paleontological tools is difficult because of the gaps in the fossil record, and because of the lack of any quantitative relation between the morphology and physiology of animals and their fitness or performance. Another difficulty arises from the inherent properties of evolution itself. Because evolution is a one-time experiment, and because it occurs on such large time-scales, evolutionary biologists are often reduced to offer tentative adaptative arguments that can hardly be proved or disproved with experiments.

In this paper, to address the question of optimality and attractiveness of designs in the fitness landscape, a different approach is proposed. The optimal shapes and motions of undulatory swimmers are computed with an evolutionary algorithm. The premises of this computation are that fluid mechanics is the main selective pressure on undulatory swimmers, and that their fitness can be assessed through two measurable performance variables: their swimming velocity and their efficiency. The goal here is to describe the optimality of undulatory swimming beyond the naive arguments of maximisation of thrust and minimisation of drag (Blake 2004).

The first to address physically the optimisation of shape in undulatory swimming is probably Lighthill (1969, 1970), using a linear elongated-body theory proposed in Lighthill (1960). From mainly inviscid considerations, Lighthill (1970) showed with a simple model that the morphology of carangiform (or salmon-like) swimmers is adapted to their motion. He argued that the localisation of the large amplitudes of motion near the tail is aimed at reducing the wasted energy due to what he called the 'vortex-force effect', which is simply the drag force due to transverse motions. Then he showed that the amplitude of the motion should be almost constant near the tail, or equivalently that the transverse velocity and the incident angle of the tail should be in phase. This means that there should be a narrow region just ahead of the tail where there is a rapid increase of the motion amplitude. To further minimise the wasted energy, he argued that the cross-section of this narrow region, which corresponds to the caudal peduncle, should be as small as possible. Finally, he showed that, since the thrust force is generated at the tail and accompanied by a lateral force, a periodic torque is produced that leads to a recoil pitching motion. To limit this inefficient recoil motion, the anterior and rigid region of the body should have a large mass or a large added-mass. In brief, using mainly linear and inviscid arguments, Lighthill (1970) showed convincingly that tuna and related

fish have a shape adapted to their swimming motion. However, these explanations lacked quantitative elements and did not take into account nonlinearities and internal mechanics.

Focusing on large thunniform swimmers belonging to the salmon-like group, Lighthill (1970) and Wu (1971*a*) calculated the optimal flapping motion of a two-dimensional rigid foil with the aim of modelling the lunate tail of these animals. They showed that, similarly to the elongated-body approximation results (Lighthill 1960, 1970; Eloy 2012), one expect the transverse velocity and the incident angle of the tail to be in phase. These optimisation calculations were later confirmed by the experiments of Triantafyllou *et al.* (1993), and, more recently, Eloy & Schouveiler (2011) extended this approach to a flexible flapping foil, calculating its optimal motion in two dimensions. Also addressing the optimal motion of an undulatory swimmer, Kern & Koumoutsakos (2006) used three-dimensional numerical simulations on an eel-shaped swimmer to find, with an evolutionary algorithm, the swimming gaits that maximise either the efficiency or the burst swimming speed. These different optimisation calculation are related to the problem at stake here, although all assumed explicitly or not that the swimmer shape is known. They were thus unable to address the link between the shape and the motion for optimal undulatory swimming.

Very recently, a study by Tokić & Yue (2012) has been published that addresses the optimal shape and motion of undulatory swimmers using an evolutionary algorithm. This study is very similar to the present one, although Tokić & Yue (2012) have given more emphasis to the modelling of muscles and less to the modelling of hydrodynamics. The similarities and differences between this work and the present study will be discussed in more details in §6.

This paper is organised as follows. First, in §2, the physical model is presented. In particular, the geometries and motions considered are discussed, and the different forces exerted on the swimmers are detailed. Then, in §3, the evolutionary algorithm used to solve the constrained bi-objective optimisation is described briefly, and in §4 the results of optimisation calculations are reported. Finally, these results are compared to experimental data on aquatic animals in §5 and discussed in the light of previous works in §6.

2. Model

2.1. *Geometry*

Consider an animal of length L swimming at constant mean velocity U in water at rest (see figure 1). The curvilinear coordinate s is defined as the distance from the head along the backbone such that s varies between 0 and L, assuming that the animal's backbone is inextensible. Each cross-section of the animal is taken as elliptic, with semi-major axis $a(s)$ along the vertical and semi-minor axis $b(s)$ along the horizontal (these two directions can be inverted for comparisons with aquatic mammals, as gravity plays no role here). For convenience, the axis $a(s)$ will indifferently be referred to as the height, depth, or span of the swimmer, the axis $b(s)$ will be called width or thickness, and the computational undulatory swimmers will also be designated as fish or animals.

The limit of small aspect ratio is considered such that the continuous functions $a(s)$ and $b(s)$ satisfy

$$0 \leqslant b(s) \leqslant a(s) \leqslant \epsilon L, \tag{2.1}$$

with $\epsilon \ll 1$. In the following, it will be more suitable to define the aspect ratio as the
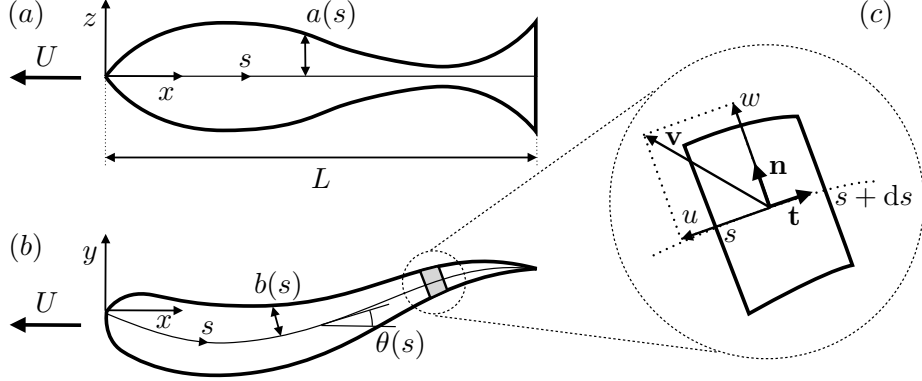
FIGURE 1. Geometry of the "animals" considered: side view (a), top view (b), and close-up (c) to show how the velocity, $\mathbf{v}$, of each cross-section is decomposed into tangential (u) and normal (w) components.

ratio of the length to the maximal major axis

$$\text{AR} = \frac{L}{2\max(a(s))}, \qquad (2.2)$$

which is equal to $\text{AR} = 1/2\epsilon$ in general. To avoid blunt leading and trailing edges, it is also required that

$$a(0) = b(0) = b(L) = 0. \qquad (2.3)$$

The volume of the animal is not constrained, but a dimensionless volume, V_0, is defined as

$$Vol = V_0 \epsilon^2 L^3, \qquad (2.4)$$

where Vol is the animal volume.

The mass per unit length is then

$$M(s) = \rho \pi a b, \qquad (2.5)$$

where ρ is the density of both water and the animal. While the added mass per unit length is

$$m(s) = \rho \pi a^2. \qquad (2.6)$$

This added mass corresponds to the equivalent mass of water displaced when a given cross-section is moved in a direction normal to the backbone (it will be used below to calculate the reactive forces). Finally, the moment of inertia associated with a rotation in the Oxy plane is

$$I(s) = \rho \frac{\pi}{4} a b^2. \qquad (2.7)$$

2.2. Kinematics

The motion of the animal is prescribed through its curvature, assumed to be harmonic of angular frequency ω

$$\theta'(s,t) = K(s) e^{i\phi(s)} e^{i\omega t}, \qquad (2.8)$$

where θ is the local incident angle as defined in figure 1b, K and ϕ are the amplitude and phase of the curvature, and the prime denotes derivation with respect to s. Note that, here, the complex notation is used, but when nonlinear terms will be involved, the real notation will be assumed. To obtain motions that are compatible with an actuated

elastic body, the bending moments and tensile forces should be zero at the head and at the tail, which translates into boundary conditions for K:

$$K(0) = K'(0) = K(L) = K'(L) = 0. \tag{2.9}$$

Integrating the prescribed curvature (2.8) yields the local incident angle θ of zero mean

$$\theta(s,t) = \left(\Theta_1 + \int_0^s K(\xi) e^{i\phi(\xi)} d\xi \right) e^{i\omega t} \equiv \theta_1(s) e^{i\psi(s)} e^{i\omega t}, \tag{2.10}$$

where Θ_1 is a constant of integration physically related to the amplitude of the pitching recoil motion. Taking the cosine and sine of the incident angle, and using formulas (9.1.44–45) in Abramowitz & Stegun (1965) gives

$$x'(s,t) = \cos\theta = J_0(\theta_1) - 2J_2(\theta_1) e^{2i\psi} e^{2i\omega t} + \cdots, \tag{2.11a}$$

$$y'(s,t) = \sin\theta = 2J_1(\theta_1) e^{i\psi} e^{i\omega t} - \cdots, \tag{2.11b}$$

where $J_n(x)$ is the Bessel function of the first kind. Integrating again gives the position of any point of the backbone in the Oxy plane

$$x(s,t) = -Ut + X_2 e^{2i\omega t} + \int_0^s x'(\xi) d\xi \equiv x_0(s) + x_2(s) e^{2i\omega t} + \cdots, \tag{2.12a}$$

$$y(s,t) = Y_1 e^{i\omega t} + \int_0^s y'(\xi) d\xi \equiv y_1(s) e^{i\omega t} + \cdots, \tag{2.12b}$$

where Y_1 and X_2 are two constants of integration associated with the amplitudes of heaving and surging recoil motions respectively. From the position (x, y) of a point on the backbone, its velocity can be determined as $\mathbf{v} = (\dot{x}, \dot{y})$, where the dots denote differentiation with respect to t. Projecting this velocity onto its tangential and normal components (figure 1c) gives

$$u = \dot{x}x' + \dot{y}y' \equiv u_0(s) + u_2(s) e^{2i\omega t} + \cdots, \tag{2.13a}$$

$$w = \dot{y}x' - \dot{x}y' \equiv w_1(s) e^{i\omega t} + \cdots, \tag{2.13b}$$

where care has to be taken with the complex notations because these expressions are nonlinear.

At this point, the full swimming kinematics is characterised by two prescribed functions, the amplitude $K(s)$ and phase $\phi(s)$ of the curvature, and seven unknown scalars: the real and imaginary parts of the recoil amplitudes Θ_1, Y_1, and X_2, and the mean swimming speed U.

The present model is based on the slender-body approximation. It is therefore valid when the aspect ratio AR is asymptotically large, or equivalently when ϵ is small. If one assumes that the first harmonic of the deflection $y_1(s)$ is also $0(\epsilon)$, then the second harmonic of the x-deflection, $x_2(s)$, will be $O(\epsilon^2)$, and the third harmonic $y_3(s)$ will be $0(\epsilon^3)$. Keeping all harmonics up to the third thus gives a model correct up to the first $O(\epsilon^2)$ nonlinear corrections. However, preliminary calculations have shown that the third harmonic could be neglected to substantially decrease the computation time, without affecting the results. All the calculations were therefore performed by keeping the mean values and the first two harmonics of all functions.

Now, three forces will be assumed to act on the swimming fish. First, a drag force will be considered, and it will be decomposed into pressure and skin-friction drags. Then, since the body is elongated, it will be assumed that reactive and resistive forces apply independently and locally on every cross-section of the animal. These forces are identical

to the ones that would apply on an infinite cylinder of same cross-section moving with the same velocity in water.

2.3. *Pressure drag*

The pressure drag, or form drag, $\mathbf{F}_p$, is generally due to the shedding of vorticity that can occur when the shape is not perfectly streamlined. For simplicity, it is assumed here that this form drag is not modified by the motion of the animal. A realistic estimation of $\mathbf{F}_p$ would require relatively long numerical calculations not compatible with the present approach. An empirical description is chosen instead, based on the formulas given by Hoerner (1965) for axisymmetric and two-dimensional streamlined rigid bodies. The empirical formula used for the pressure drag reads

$$\mathbf{F}_p = \frac{1}{2}\rho U_0^2 \times 0.33 \frac{B}{L} S_f\, \mathbf{e}_x, \qquad (2.14)$$

where $\mathbf{e}_x$ is the unit vector in the x-direction, U_0 is the mean tangential velocity at the head satisfying

$$U_0^2 = u_0^2(0) + \frac{1}{2}|u_2(0)|^2, \qquad (2.15)$$

with u_0 and u_2 defined by (2.13), S_f has the dimension of a surface and is given by

$$S_f = \frac{\pi}{4}ABS^*, \qquad (2.16)$$

with A and B the maximal height and width of the fish such that

$$A = 2\max(a), \quad B = 2\max(b), \qquad (2.17)$$

and S^* is an empirical dimensionless number that describes the streamlining of the function $b(s)$, and which is given by

$$S^* = \int_0^L \frac{|b'|^2 bL}{B^3}\left(5.2 - 4.4\,\mathrm{sgn}(b')\right)\,\mathrm{d}s. \qquad (2.18)$$

The surface S_f is thus equal to the maximal cross-section, $\pi AB/4$, multiplied by this dimensionless factor S^*. As illustrated in figure 2, S^* is minimal and equal to 1.0 when the profile is streamlined and increases as streamlining worsen. By setting $S^* = 1$ and $A = B$, the formula (2.14) becomes identical to the empirical approximation of Hoerner (1965) for axisymmetric streamlined bodies. When $S^* = 1$ and $A \gg B$, one recovers, the empirical formula of Hoerner (1965) for two-dimensional airfoils. The formula (2.18) for S^* aims at extending these empirical formulas to non-streamlined bodies. It is somewhat tentative and would need to be confirmed and fine-tuned with specific studies in the future. Although this approach to model pressure drag may not be rigorous, one can also consider it as a penalisation method. When the profile $b(s)$ is not exactly as pictured in figure 2a, the drag increases and the shape is penalized. As it will be seen below, optimal solution rarely correspond to the minimum $S^* = 1$, expressing that the optimal shape is a balance between streamlining and other important features related to the form such as inertia and viscoelastic dissipation.

2.4. *Skin-friction drag*

The skin-friction drag is different when the animal is in motion or not. When there is no motion, it can be estimated using Mangler's transformation (see Schlichting 1979,
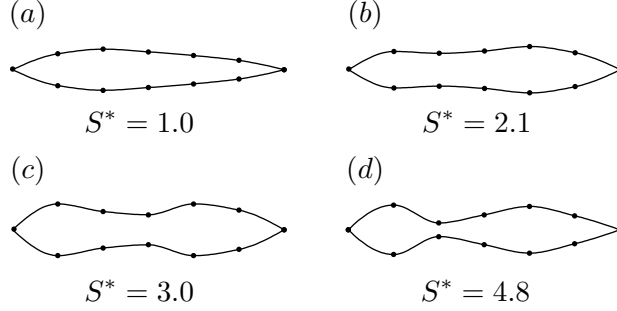
(a)

(b)

$S^* = 1.0$

$S^* = 2.1$

(c)

(d)

$S^* = 3.0$

$S^* = 4.8$

FIGURE 2. Illustration of the values taken by S^*, as given by (2.18), for different profiles $b(s)$. These profiles are obtained by a cubic spline interpolation around 5 degrees of freedom regularly spaced between the leading and the trailing edge (the black dots). The first case (a) corresponds to the minimal value of S^*, and the other three (b–d) are random cases illustrating the link between streamlining and low values of S^*.

p.245–247), which gives the laminar skin friction on an axisymmetric body

$$\mathrm{d}\mathbf{F}_\mu = 0.332\rho U_0^2 \left(\mathrm{Re}\frac{U_0}{U}\right)^{-\frac{1}{2}} \frac{\ell}{\left(\int_0^s \ell^2 \mathrm{d}s\right)^{\frac{1}{2}}} 2\pi\ell\,\mathrm{d}s\,\mathbf{t}, \qquad (2.19)$$

where $\mathbf{t}$ is the tangential unit vector oriented as in figure 1c,

$$\mathrm{Re} = UL/\nu, \qquad (2.20)$$

is the Reynolds number, and $\ell(s)$ is the radius of an equivalent body of revolution, taken to be

$$\ell(s) = \frac{2}{\pi}aE\left(1 - \frac{b^2}{a^2}\right), \qquad (2.21)$$

with E the complete elliptic integral of the second kind. This choice of ℓ gives a perimeter, $2\pi\ell$, equal to the perimeter of the elliptic cross-section of the fish. To calculate the skin-friction $\mathrm{d}\mathbf{F}_\mu$, it has also been assumed that the outer velocity is everywhere U_0, which is of course not exactly true, but is a convenient approximation. The total skin friction calculated by integrating (2.19), when added to the pressure drag given by (2.14), gives the total drag when the animal is motionless. This total drag compares very well with the empirical formulas given by Hoerner (1965) in the case of axisymmetric streamlined bodies. The present approach is however preferable because it allows one to calculate not only the total drag, but also the distribution of the skin friction along the length of the animal.

When the fish is moving, the boundary layers are modified and the skin-friction drag can be enhanced (e.g. Ehrenstein & Eloy 2012). This enhancement is intimately due to the compression of the boundary layer in the presence of crossflow, a phenomenon sometimes referred to as the 'Bone-Lighthill boundary-layer thinning' mechanism in reference to a remark made by Lighthill (1971) citing a conversation with Bone. The precise modelling of this effect is still an open problem today, but it can be approximated by the formula of Taylor (1952) for a smooth circular cylinder in steady flow, which yields, after time-averaging, to the force per unit length

$$\mathrm{d}\mathbf{F}_\nu = -2.9\rho|\nu a w_1|^{1/2} u_0\,\mathrm{d}s\,\mathbf{t}, \qquad (2.22)$$

where the second harmonic (i.e. the term proportional to $\mathrm{e}^{2\mathrm{i}\omega t}$) has been neglected, and it has been assumed that $b(s)$ has no influence. This latter assumption is consistent with

the experimental observations of Ota & Nishiyama (1984) on the heat transfer around an elliptic cylinder in crossflow (as already pointed out by Taylor 1952, there is an analogy between the two problems), but not exactly with the boundary layer calculations of Ehrenstein & Eloy (2012). Because of the square root dependence with lateral velocity w_1, $\mathrm{d}\mathbf{F}_\nu$ accounts for the increase of skin friction due to the motion of the animal as observed experimentally by Anderson *et al.* (2001) and numerically by Borazjani & Sotiropoulos (2008).

To take into account the situations where the skin-friction drag for a motionless animal, $\mathrm{d}\mathbf{F}_\mu$, and the skin-friction drag due to motion, $\mathrm{d}\mathbf{F}_\nu$, are of same order, the total skin-friction drag is taken to be

$$\mathrm{d}\mathbf{F}_\parallel = \mathrm{d}\mathbf{F}_\mu \mathrm{e}^{-4|w_1/U|} + \mathrm{d}\mathbf{F}_\nu, \qquad (2.23)$$

which ensures that $\mathrm{d}\mathbf{F}_\parallel = \mathrm{d}\mathbf{F}_\mu$ when there is no lateral motion, i.e. $w_1 = 0$, and $\mathrm{d}\mathbf{F}_\parallel \approx \mathrm{d}\mathbf{F}_\nu$ when w_1 is large. This *ad hoc* formulation captures the essential features of the skin-friction drag, in particular the effect of skin-friction enhancement due to transverse motion. Preliminary studies have shown that, as long as this specific effect is conserved, the results remains essentially the same when a different model for skin-friction drag is used.

This model of the skin-friction drag corresponds to laminar boundary layers and is thus applicable up to Reynolds numbers $\mathrm{Re} \approx 10^6$. Beyond this limit, the boundary layers will likely be turbulent even if most swimming animals use ingenious mechanisms to delay this transition such as the release of secretions through their skins (Rosen & Cornford 1971; Hoyt 1975). In the case of turbulent boundary layers, one could devise a specific skin-friction model using an approach similar to the one used here for laminar ones. However, this would involve additional modelling assumption, and, for the sake of simplicity, the study has been restricted to the case of laminar skin friction, which already allows one to address swimming optimisation up to fish lengths of the order of $L = 30\,\mathrm{cm}$.

2.5. *Dynamics*

In addition to the drag, reactive and resistive forces also act on the swimming fish. The reactive force has been first formulated by Lighthill (1971) in the case of large amplitude swimming. From a physical point of view, it results from the acceleration of an added mass of fluid when the animal is moving. To accelerate this mass of water, a force has to be applied to it, and reactively the opposite force is exerted on the swimming animal. Recently, Candelier *et al.* (2011) have given a more rigorous proof of Lighthill's result, and complemented it with comparisons with numerical results. On every cross-section of thickness $\mathrm{d}s$ (see figure 1c), this reactive force can be written as

$$\mathrm{d}\mathbf{F}_m = \partial_s \left(mwu\mathbf{n} - \tfrac{1}{2}mw^2\mathbf{t} \right) \mathrm{d}s - \partial_t \left(mw\mathbf{n} \right) \mathrm{d}s, \qquad (2.24)$$

where $\mathbf{t}$ and $\mathbf{n}$ are the tangential and normal unit vectors (figure 1c). The expression (2.24) derives from the conservation of momentum applied to a slice of fluid attached to the cross-section $[s \quad s+\mathrm{d}s]$. The first term of (2.24) corresponds to the flux of momentum through the fluid slice, the second to the pressure forces and the last to the rate of change of momentum. It can be seen that the total reactive force, obtained by integrating (2.24) between $s = 0$ and L, is a sum of a term that depends only on the motion of the tail (as $m = 0$ in $s = 0$) and a term of zero time-average. This remarkable feature, already pointed out by Lighthill (1971), has recently been used to calculate the optimal motion of the tail in the inviscid limit (Eloy 2012).

The large-amplitude elongated-body theory of Lighthill (1971) takes advantage of the

large aspect ratio of the swimming animal to assume that the flow (and the reactive force) at a given section does not depend on the animal's motion at other sections. In particular the vorticity shed in the wake has no influence on the reactive force in this large aspect ratio limit. If one wanted to model manoeuvres such as turns and start, or the hydrodynamical interactions within a fish school, Lighthill's theory would have to be refined to take into account these effects.

The above discussion on the kinematics suggests that the present model is correct up to the first nonlinear corrections, of order ϵ^2 smaller than the leading order. However, the nonlinear corrections on the reactive force due to a moderate aspect ratio have been neglected in the analysis. This effect would give an additional nonlinear term of order $\epsilon^2 \ln(\epsilon)$ as it has been shown in Eloy *et al.* (2010). It is beyond the reach of the present paper to include this term and it has thus been assumed to be negligible, but it would certainly be interesting to assess the validity of this assumption in the future.

The resistive force, which is the component of the drag normal to the backbone when the lateral velocity is non zero can be expressed as

$$d\mathbf{F}_\perp = -\frac{8}{3\pi} C_D a \rho w_1 |w_1| e^{i\omega t}\, ds\, \mathbf{n}, \qquad (2.25)$$

where only the first harmonic has been kept (the $8/3\pi$ factor above comes from projecting $w|w|$ onto the harmonic $e^{i\omega t}$), and where $C_D = 2 - b/a$ is a linear approximation of the drag coefficient of the elliptic cross-section when moving parallel to its minor axis.

Now that the different forces acting on the fish have been expressed (pressure drag $\mathbf{F}_p$, skin-friction drag $d\mathbf{F}_\parallel$, reactive force $d\mathbf{F}_m$, and resistive force $d\mathbf{F}_\perp$), Newton's second law can be used. Conservation of momentum and angular momentum can be expressed as

$$\mathbf{F}_p + \int_0^L d\mathbf{F}_m + d\mathbf{F}_\perp + d\mathbf{F}_\parallel - M\ddot{\mathbf{r}} ds = 0, \qquad (2.26a)$$

$$\int_0^L I\ddot{\theta}\mathbf{e}_z ds + (d\mathbf{F}_m + d\mathbf{F}_\perp + d\mathbf{F}_\parallel - M\ddot{\mathbf{r}} ds) \times \mathbf{r} = 0, \qquad (2.26b)$$

where $\mathbf{r} = (x, y)$ is the position vector. The projection of $(2.26a)$ onto the x-direction only involves even harmonics. Keeping terms up to second harmonic yields three equations (one for the time-average and two for the real and imaginary parts of the second harmonic). On the contrary, the projection of $(2.26a)$ onto the y-direction involve odd harmonics, and keeping only the first harmonic yields two other equations. Finally, the first harmonic of $(2.26b)$ gives the two last equations. Therefore, the equations $(2.26a)$ and $(2.26b)$, when projected adequately, give the seven equations needed to calculate unambiguously the seven unknowns of the kinematics evoked above.

Note that, this system of equations is fully coupled and nonlinear, and, as a consequence, there is no simple analytical way of inverting it. In the present work, the function `fsolve` of MATLAB is used to solve this system numerically by discretising the integrals in $(2.26a$–$b)$ on 100 collocation points. This computation generally takes about 0.1 s on a laptop computer.

For a shape set by the functions $a(s)$ and $b(s)$, and a motion given by $K(s)$ and $\phi(s)$, the recoil motion and the mean swimming speed can be calculated. To fully address the swimming performances, the energetic costs have now to be computed as well.

2.6. *Energetics*

The average power needed to perform the prescribed motion (labeled 'e' as external) is given by

$$P_e = \mathbf{F}_p \cdot U\mathbf{e}_x + \langle \int_0^L \left(d\mathbf{F}_m + d\mathbf{F}_\perp + d\mathbf{F}_\parallel \right) \cdot \mathbf{v} \rangle, \qquad (2.27)$$

where the brackets denotes time-averaging. As shown by Lighthill (1971), the reactive part of this power simplifies to

$$P_m = \langle \int_0^L d\mathbf{F}_m \cdot \mathbf{v} \rangle = \left[\tfrac{1}{2} m \langle w^2 u \rangle \right]_{s=L}, \qquad (2.28)$$

which corresponds physically to the kinetic energy given to the wake per unit time.

In addition to this energetic cost of hydrodynamical origin, an internal dissipation has been considered by assuming that the fish soft tissues are viscoelastic such that the power dissipated internally is

$$P_i = \langle \int_0^L \tfrac{1}{2} \mu_i I |\dot{\theta}'|^2 ds \rangle, \qquad (2.29)$$

where μ_i is the dynamic viscosity of the material, several orders of magnitude larger than the viscosity of water. The precise value taken by μ_i for different species of aquatic animals is largely an open question and is discussed in appendix C. From this internal viscosity, an internal Reynolds number can be defined,

$$\mathrm{Re}_i = \frac{\rho U L}{\mu_i}, \qquad (2.30)$$

which measures the relative importance of hydrodynamical energy losses and internal dissipation. The total average power needed to swim is the sum of the external and internal powers

$$P_{\text{tot.}} = P_e + P_i. \qquad (2.31)$$

2.7. *Dimensionless numbers*

To analyse the results in a proper manner, dimensionless quantities are now introduced. The energetic costs are measured through a dimensionless efficiency

$$E^* = \frac{\rho \, Vol^{2/3} U^3}{P_{\text{tot.}}}. \qquad (2.32)$$

It measures the distance that can be travelled by a unit mass fish with unit energy ($\rho U \, Vol / P_{\text{tot.}}$ in $\mathrm{m\,kg\,J^{-1}}$) made dimensionless by the characteristic acceleration $U^2 / Vol^{1/3}$. Note that the acceleration of gravity is not used here, since it plays no role in the problem. The efficiency E^* can also be seen as a dimensionless 'gas mileage' and is similar to the inverse of a 'cost of transport' (Tucker 1970; Videler 1993).

If one believes that the available power of a given animal is proportional to its volume to the power 2/3, the efficiency E^*, given by (2.32), is also a measure of the ratio of the available power to the actual power spent. In fact, Kleiber's law states that the metabolic rate of animals is proportional to $Vol^{3/4}$, and not $Vol^{2/3}$, but the question of the validity of this scaling law is still controversial (e.g. Dodds *et al.* 2001; White & Seymour 2005), and, in any case, this slightly different exponent would not qualitatively change the results of the present analysis.

The dimensionless number that characterise the mean swimming velocity is the stride

	Symbol	Formula	Equation	Name
Shape	AR	$L/\max(a)$	(2.2)	aspect ratio
	V_0	$Vol/(\epsilon^2 L^3)$	(2.4)	volume
	$b_{\min}$	$\min(b_i/L)$	–	minimal thickness
Motion	$\theta_{\max}$	$\|\theta_1(L)\|$	(2.10)	tail maximum incident angle
	U/V	U/V	(2.39)	slip ratio
	St	fA/U	(2.34)	Strouhal number
Physical	Re	UL/ν	(2.20)	Reynolds number
	Re_i	$\rho UL/\mu_i$	(2.30)	internal Reynolds number
	I_p	$D_p/(D_p + D_\parallel)$	(2.35)	fraction of form drag
	I_D	D/D_{plate}	(2.35)	first drag index†
	I_w	D/D_{rigid}	(2.35)	second drag index‡
Performance	E^*	$\rho Vol^{2/3}U^3/P_{\text{tot.}}$	(2.32)	efficiency
	U^*	U/fL	(2.33)	stride length
	Li	$D/(2\rho a^2(L)U^2)$	(2.38)	Lighthill number
	I_m	$T_{\text{reac.}}/(T_{\text{reac.}} + T_{\text{resis.}})$	(2.37)	thrust index

† With D_{plate} the drag of a flat plate of same surface S.
‡ With D_{rigid} the drag of the motionless animal.

TABLE 1. Dimensionless parameters

length which is the number of fish lengths travelled during one tailbeat period

$$U^* = \frac{U}{fL} = \frac{2\pi U}{\omega L}, \tag{2.33}$$

where f is the tailbeat frequency.

A commonly used dimensionless number to characterise the amplitude and frequency of the tail motion is the Strouhal number

$$\text{St} = \frac{fA}{U} = \frac{\omega\, y_1(L)}{\pi U}, \tag{2.34}$$

where A is the peak-to-peak amplitude at the tail.

One can also define the total drag D as the sum of the pressure drag $\mathbf{F}_p$ defined above and the average contribution of the tangential component of the viscous stresses $\mathrm{d}\mathbf{F}_\parallel$ such that

$$D = \left(\mathbf{F}_p + \langle\int_0^L \mathrm{d}\mathbf{F}_\parallel\rangle\right)\cdot\mathbf{e}_x \equiv D_p + D_\parallel, \tag{2.35}$$

where D_p is the form drag and $D_\parallel$ is the skin-friction drag. Three indexes are then defined: $I_p = D_p/(D_p + D_\parallel)$ is the ratio of form drag to total drag; I_D is the ratio of the total the drag to the drag of a flat plate of same surface assuming Blasius boundary layers (Schlichting 1979); and I_w is the ratio of the total drag to the drag of the same body without motion.

Similarly the total contribution to the energetic costs can be divided into several components:

$$P_{\text{tot.}} = \left(\mathbf{F}_p\cdot U\mathbf{e}_x + \langle\int_0^L \mathrm{d}\mathbf{F}_\parallel\cdot\mathbf{v}\rangle\right) + \langle\int_0^L (\mathrm{d}\mathbf{F}_m + \mathrm{d}\mathbf{F}_\perp)\cdot\mathbf{v}\rangle + P_i \tag{2.36a}$$

$$\equiv P_D + P_m + P_\perp + P_i, \qquad (2.36b)$$

with P_D the contribution of the total drag, P_m the inviscid or reactive energetic cost, $P_\perp$ the resistive cost of perpendicular motion, and P_i is the internal viscoelastic dissipation given by (2.29).

To quantify the relative importance of reactive and resistive forces to generate thrust, the index I_m is defined as

$$I_m = \frac{\mathbf{e}_x \cdot \int_0^L \mathrm{d}\mathbf{F}_m}{\mathbf{e}_x \cdot \int_0^L \mathrm{d}\mathbf{F}_m + \mathrm{d}\mathbf{F}_\perp}, \qquad (2.37)$$

such that it measures the relative importance of reactive forces to generate thrust.

An important dimensionless quantity can also be constructed that measures the ratio of the drag D to the typical available reactive thrust. Following a previous article (Eloy 2012), this quantity is called the Lighthill number and is equal to

$$\mathrm{Li} = \frac{\pi D}{2m(L)U^2} = \frac{1}{2}\frac{D}{\rho a^2(L)U^2}. \qquad (2.38)$$

To characterise the motion, the wave speed V of the deformation at the tail is also defined, and it is measured on the posterior 10%. The slip ratio U/V is then given by

$$\frac{U}{V} = \frac{10\,U}{\omega L}\arg\left(\frac{y_1(0.9L)}{y_1(L)}\right). \qquad (2.39)$$

For convenience, the dimensionless parameters that characterise the problem are gathered in Table 1.

3. Evolutionary algorithm

For a given shape, described by the functions $a(s)$ and $b(s)$, and a given motion described by $K(s)$ and $\phi(s)$, the model described above allows one to calculate the full dynamics, in particular the recoil motion and the mean swimming speed. The performances of the animal are then deduced from this dynamics. In particular two dimensionless functions, the efficiency or distance E^* and the stride length U^*, can be calculated.

The main goal of the present paper is to find the shapes and the associated motions that maximise E^*, or U^*, or any trade-off between the two. Mathematically, a bi-objective constrained optimisation has to be solved. The complexity of this problem and the relatively large number of degrees of freedom involved call for the use of an evolutionary algorithm. In the following, the principle of this algorithm will be briefly explained.

3.1. Discretisation

In order to characterise the functions a, b, K, and ϕ with a limited number of degrees of freedom, the values of these functions are prescribed on node points spaced regularly along the curvilinear coordinate s. In other words, the segment $[0 \quad L]$ is divided into N equal segments such that the degrees of freedom are the values taken by a, b, K, and ϕ at $s_i = iL/N$ (with $i = 0 \dots N$). These values will be noted a_i, b_i, K_i, and ϕ_i in the following.

Some geometrical and dynamical restrictions apply to these degrees of freedom. More specifically, to avoid blunt leading and trailing edges, and to ensure that the motion is compatible with an activated elastic body, the following constraints apply

$$a_0 = b_0 = K_0 = \phi_0 = 0, \quad b_N = K_N = 0. \qquad (3.1)$$

Given the $N + 1$ nodes for each of the 4 functions and the 6 additional constraints, the

number of degrees of freedom is $4N - 2$. In order to avoid infinitely thin cross-sections, a minimal value for the semi-axes of the ellipses is also assumed

$$0.15\,\epsilon L \leqslant b_i \leqslant a_i \leqslant \epsilon L \quad \text{for } i = 1 \ldots N - 1, \tag{3.2a}$$

$$0 \leqslant a_N \leqslant \epsilon L. \tag{3.2b}$$

The amplitude and phase of the curvature are also constrained

$$0 < K_i < 10/L \quad \text{for } i = 1 \ldots N - 1, \tag{3.3a}$$

$$-\pi < \phi_{i+1} - \phi_i \ < \pi \qquad \text{for } i = 1 \ldots N - 1. \tag{3.3b}$$

These constraints are generally not reached during the optimisation and only serve to give the order of magnitude of the K_i's and ϕ_i's. Between the node points, s_i, the functions a, b, K, and ϕ are interpolated with a cubic spline function. For the curvature $K(s)$, the first derivative should be zero in $s = 0$ and L as stated by (2.9). This is ensured by adding two node points in $0.01L$ and $0.99L$ where K is zero.

The shape and swimming gait are now described by $4N - 2$ real numbers. Each of them is called a gene and is constrained by the inequalities $(3.2a,b)$ and $(3.3a,b)$. The vector containing all the genes is called the genome of a given individual and denoted by

$$\mathbf{G} = (a_1 \ldots a_N, b_1 \ldots b_{N-1}, K_1 \ldots K_{N-1}, \phi_1 \ldots \phi_N). \tag{3.4}$$

Through the model described in § 2, the performances associated with a given genome can be calculated. In particular the functions $E^*(\mathbf{G})$ and $U^*(\mathbf{G})$, which correspond to the dimensionless efficiency and velocity of swimming respectively, can be computed.

3.2. *Principle*

The evolutionary algorithm used in the present study is adapted from the PESA-II method of Corne *et al.* (2001). Its principle will be briefly explained now (Branke *et al.* 2008, provide a general review on this subject).

First, two important concepts pertaining to multi-objective optimisation are introduced: the dominance and the Pareto front. In the U^*–E^* plane, called the objective space, the domain accessible by all individual will be noted $\mathcal{D}$ as illustrated in figure 3a. To compare two individuals, the concept of *dominance* in $\mathcal{D}$ is used. An individual of genome $\mathbf{G}_1$ is said to *dominate* an individual of genome $\mathbf{G}_2$ if one of the two following conditions is true

$$U^*(\mathbf{G}_1) > U^*(\mathbf{G}_2), \quad E^*(\mathbf{G}_1) \geqslant E^*(\mathbf{G}_2), \quad \text{or} \tag{3.5a}$$

$$U^*(\mathbf{G}_1) \geqslant U^*(\mathbf{G}_2), \quad E^*(\mathbf{G}_1) > E^*(\mathbf{G}_2). \tag{3.5b}$$

The set of all non-dominated points of $\mathcal{D}$ is called the *Pareto front* and appears in bold in figure 3a. The goal of the evolutionary algorithm is to best approach this Pareto front.

The algorithm is illustrated by the flowchart reproduced in figure 4. The main principle is to keep, at all times, both an active population, which is evolved at each time step, and an *archive*, which contains the best approximation of the Pareto front at each generation. More precisely, the different steps consist in the following:

(a) *Creation of the population:* P genomes $\mathbf{G}_i$'s that satisfy the constraints (3.2–3.4) are first selected at random. These P genomes constitute the initial active population, noted $\mathcal{P}$.

(b) *Evaluation of the population:* Each individual of $\mathcal{P}$ is evaluated, i.e. $U^*(\mathbf{G}_i)$ and $E^*(\mathbf{G}_i)$ are calculated for $i = 1 \cdots P$.

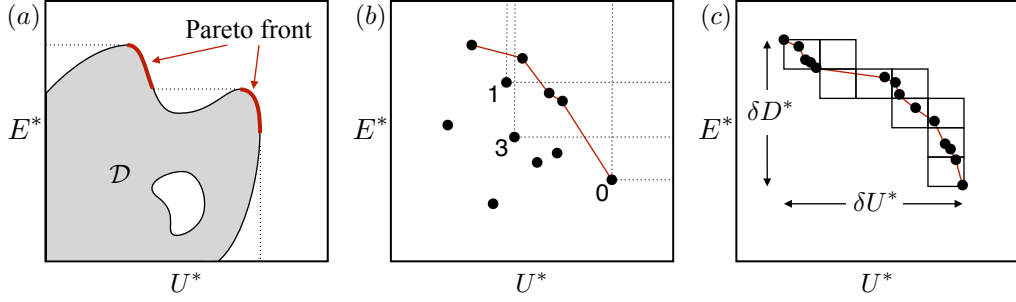(c) *Ranking of the population:* Once the active population is evaluated, a rank can be

FIGURE 3. Illustration of the principles of the evolutionary algorithm: (*a*) The Pareto front is the set of non-dominated points in the plane U^*–E^*; (*b*) A rank can be assigned to each individual by counting the number of other individuals dominating them (the labels indicate examples of ranks on three individuals). The individuals of rank 0 form the archive (solid line), which is the best approximation of the Pareto front, i.e. the set of non-dominated individuals; (*c*) To constitute the mating pool, the archive of dimension $\delta U^* \times \delta P^*$ is divided into boxes of dimensions $(3\delta U^*/P) \times (3\delta P^*/P)$ from which individuals are taken at random.

associated with each individual of genome $\mathbf{G}_i$. As illustrated in figure 3*b*, the rank $r(i)$ is simply the number of individuals dominating the i-th individual.

(*d*) *Creation of the archive:* For the first generation, the archive is simply the set of individuals of rank 0. At this step, the number of individuals in the archive is between 1 and P, because there is always at least one non-dominated individual. The archive corresponds to the current approximation of the Pareto front.

(*e*) *Creation of the mating pool:* A 'mating pool' of size P is created from the current archive and population. First, the archive set is divided into equal-size boxes as illustrated in figure 3*c*. In each of these non-empty boxes a random individual is taken and added to the mating pool and given a rank of zero. The mating pool is completed by individuals of the active population, starting with individuals of rank zero, and proceeding with increasing rank number. The goal of this procedure is to avoid cluster of points on the archive. When the archive is sufficiently populated, the mating pool is composed from individuals originating from the archive for approximately one half, and individuals originating from the active population for the other half.

(*f*) *Update of the population:* From the mating pool, a new active population is created as follows. With a probability p_{mutate}, two individuals are taken at random from the mating pool, and a tournament is run between them, i.e. the individual with the lowest rank is selected or the choice is made at random if they are of equal rank. The chosen individual is then mutated, which means that, with a probability p_m, every gene of its genome is modified by an amount given by a normal distribution of standard deviation $\delta_m \Delta g$, where p_m and δ_m are adjustable parameters, and Δg is the typical order of magnitude of the gene, given by the bounds in (3.2*a*,*b*) and (3.3*a*,*b*). With a probability $p_{\text{mate}} = 1 - p_{\text{mutate}}$, two individuals are selected from two pairs taken from the mating pool after a tournament round. From these two individuals, the parents, a new individual, a child, is created. The genes of the child are taken at random between the parent values, with a probability p_c, or equal to the mother's gene with a probability $1 - p_c$ (the mother is simply one of the parent chosen arbitrarily). Then, the genes of this child are mutated of a standard deviation $\delta_m \Delta g$ with a probability p_m. After all the individuals of the population are created either trough mutation alone or mating and mutation, the constrains (3.2*a*,*b*) are enforced.

(*g*) *Evaluation of the population:* As in step (*b*), the active population is evaluated.

(*h*) *Update of the archive:* The population and the archive are added up and ranked.
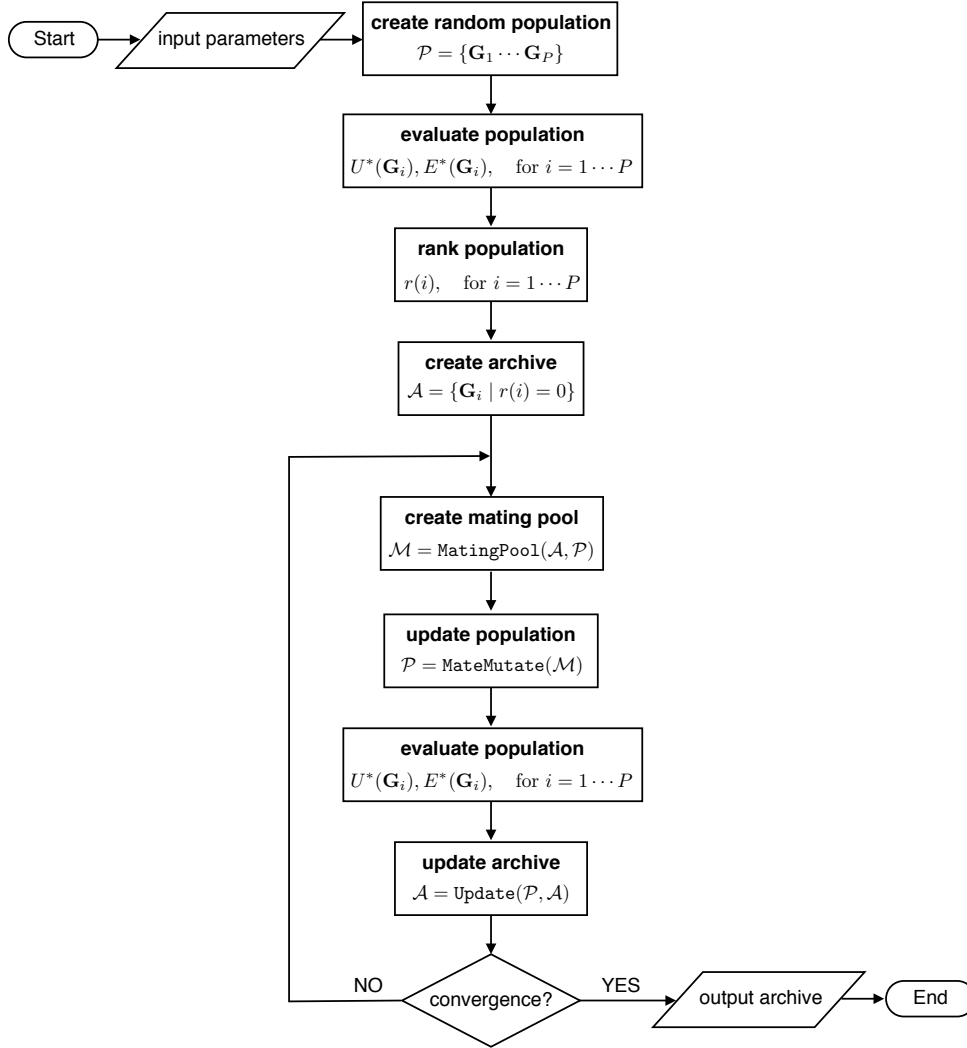
FIGURE 4. Flowchart illustrating the evolutionary algorithm.

From this super-set, the individuals of rank zero define the new archive. If the population of the archive exceeds a certain value $N_{\mathcal{A}}$, individuals of the archive are deleted in regions of largest density.

Steps $(a–d)$ constitute the initialisation of the algorithm while, the steps $(e–h)$ taken together form the main loop, which is repeated typically several thousands of times.

The parameters used for the evolutionary algorithm are summarised in Table 2. In general, the algorithm starts with a small population, $P = 15$, and a large value of the standard deviation for mutations, $\delta_m = 0.1$. As time increases the population is slowly increased up to $P = 500$, and the standard deviation decreased to $\delta_m = 0.02$ after about 10,000 generations. To avoid missing an optimum, the first 100 generations are run 10 times with different random initial population, and then gathered in a single archive. Good convergence is usually reached after about 10,000 generations, which takes approximately one day on a basic laptop computer. After that, performances cannot be improved by more than 1%.

Parameter	Symbol	Value
Size of the population	P	15–500
Maximum size of the archive	$N_{\mathcal{A}}$	10,000
Probability of non-mating	p_{mutate}	0.5
Probability of mutation of a gene	p_m	0.5
Dimensionless std for mutations	δ_m	0.02–0.1
Probability of cross-over during mating	p_c	0.5

TABLE 2. Parameters of the evolutionary algorithm.

The relative rapidity of this algorithm comes from the rapid evaluation of a single indi-
vidual. This allows one to run different optimisation calculations with different physical
parameters as it will be shown below.

4. Results

In this section, the results of the shape and motion optimisation will be discussed.
First, a set of physical parameters will be chosen to define a "reference case", and then,
these physical parameters will be varied one by one in a series of parametric studies to
study their influence on the optimal swimmer characteristics and on their performances.

4.1. Reference case

For the reference case, the Reynolds number is $\mathrm{Re} = 10^5$, the aspect ratio is $\mathrm{AR} = 6$, the
number of collocation points for each function is $N = 6$ (which gives a number of degrees
of freedom equal to $4N - 2 = 22$), and the internal viscosity is $\mu_i = 10^4\,\mathrm{Pa\,s}$, such that
the internal Reynolds number is $\mathrm{Re}_i = 10^{-2}$.

With these parameters fixed, the evolutionary algorithm described in the previous sec-
tion can be used to find the Pareto front, i.e. the set of non-dominated individuals in the
U^*–E^* plane. This numerical optimisation is illustrated in figure 5. The initial popula-
tion of 15 individuals is represented as crosses. These individuals have been selected at
random with the only constraint of having a stride length $U^* > 0.1$. After 20 generations
(which takes about one minute), one can see that the Pareto front has already greatly
improved. And after 100 generations, the approximation of the Pareto front is already
within 20% of its final value. Finally, after about 50,000 generations, one obtains an ap-
proximation of the Pareto front represented as a thick solid line in figure 5. This Pareto
front exhibits two lobes, one for velocities in the range $0.70 < U^* < 1.23$ and the other
for the range $1.23 < U^* < 2.5$.

Now, the characteristics and performances of the optimal swimmers found on this
Pareto front are examined. As illustrated in figure 5, six different individuals have been
extracted from the Pareto front, and their shapes and swimming motions are reproduced
in figures 6 and 7, while their characteristics are summarised in table 3. The first striking
feature is that the shapes of these optimal swimmers do not vary continuously along
the Pareto front. There is a abrupt change in shape between the fish labeled c and
d in figure 5. As it will be seen below, these different shapes are also associated with
qualitatively different swimming mechanisms.

The most efficient swimmers (i.e. the ones with the largest efficiencies E^*) correspond-
ing to the first lobe of the Pareto front in figure 5, have shapes and motions that bear
similarity with salmon-like fish such as tunas, cods, bass, etc. Their anterior section
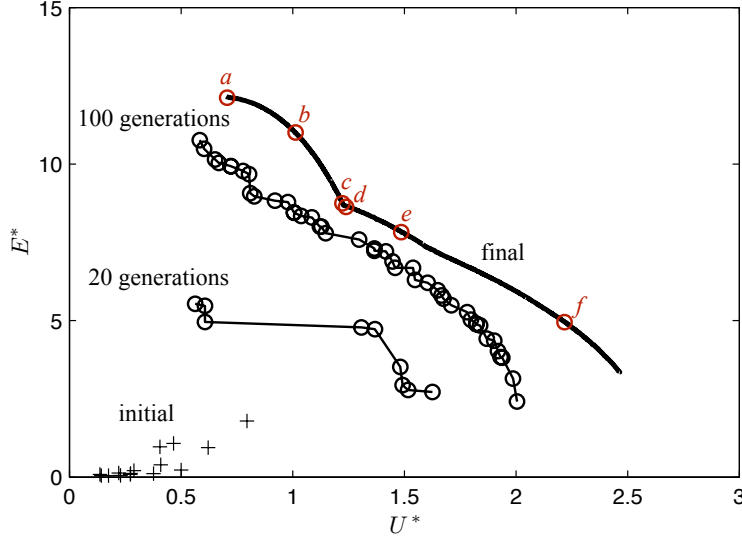gathers most of the fish mass, but is rigid during the swimming motion. This large ante-

FIGURE 5. Result of the optimisation in the U^*–E^* plane. The crosses show the initial population (selected at random with the constraint $U^* > 0.1$) and the circles mark the approximation of the Pareto front after 20 and 100 generations, as labelled. The thick black line shows the final Pareto front after about 50,000 generations and the red (grey) circles on this line correspond to particular swimmers pictured in figure 6 and whose performances are reported in table 3 (the labels are the same as the ones used in figure 6a–f).

Figure		$6a$	$6b$	$6c$	$6d$	$6e$	$6f$
Results	E^*	12.150	11.007	8.754	8.667	7.849	4.975
	U^*	0.702	1.011	1.222	1.232	1.484	2.215
	St	0.229	0.271	0.303	0.225	0.254	0.420
	Li	0.117	0.114	0.113	0.085	0.081	0.084
	$\theta_{\max}$	0.462	0.614	0.721	0.542	0.617	0.987
	U/V	0.632	0.700	0.729	0.757	0.751	0.666
	V_0	0.852	0.795	0.758	0.310	0.269	0.242
	I_p	0.220	0.195	0.181	0.088	0.072	0.070
	I_D	2.751	2.705	2.715	2.642	2.600	2.590
	I_w	1.623	1.677	1.732	2.053	2.096	2.180
	L/B	9.443	10.114	10.412	19.967	25.403	40.000
	S^*	1.363	1.333	1.282	1.621	1.952	4.018
	I_m	0.928	0.993	1.122	0.832	0.865	0.941

TABLE 3. Results for the reference case. Parameters are: $\mathrm{Re} = 10^5$, $\mathrm{AR} = 6$, $N = 6$, $\mu_i = 10^4\,\mathrm{Pa\,s}$.

rior region is separated from a thin caudal fin by a region of reduced cross-section that concentrates all the curvature during the swimming motion. Between the most efficient fish (labelled a in figures 5 and 6) and the last fish of this first lobe of the Pareto front (labelled c in figures 5 and 6), the changes in shape are only minor. However, these swimmers differ in that their amplitude of motion increases with stride length. It thus means that, with the same shape, a given fish can almost double its stride length by tuning the amplitude of its motion. This increase is accompanied by a 40% increase of energetic costs however. Together with the beat frequency, this gives a mechanism to adapt the swimming gait to the needs.
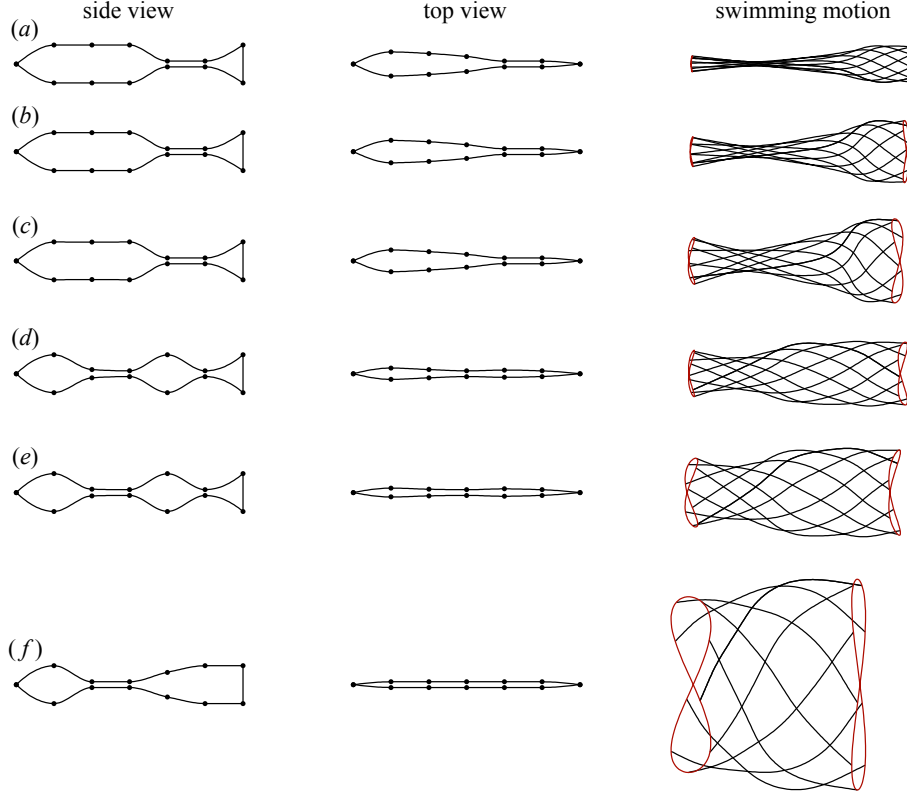
C. Eloy

FIGURE 6. Geometry and kinematics of the optimal swimmers in the reference case. Each line (*a–f*) corresponds to a different optimum on the Pareto front of figure 5 as labelled (the same examples have been taken in table 3). The first column depicts the shape with a lateral view and thus corresponds to $a(s)$, while the second column is a dorsal or top view and corresponds to $b(s)$. The black dots on these shapes are the imposed values from the genome, the rest of the shape being interpolated with cubic splines between these points. The last column depicts the deformation of the backbone during one period in the framework moving at velocity U, the black line being the backbone at different instants and the red (grey) line being the path followed by the leading and trailing edges.

The fastest swimmers, i.e. the ones with the largest dimensionless velocity U^* corresponding to the second lobe of the Pareto front in figure 5, are qualitatively different from the efficient swimmers described above. Their shape is more elongated (as seen from the dorsal view) and their swimming gaits exhibit large curvatures all along the backbone. Among these elongated swimmers, one can distinguish two different shapes: one corresponding to moderately large velocities (figure 6*d,e*); the other corresponding to very large swimming velocities (figure 6*f*). As illustrated in figure 7, these fastest swimmers use a gait different from the most efficient ones. Their slender body follows an undulating path that resemble a sinusoid, each cross-section following the preceding one along that path, as seen in the laboratory frame.

The sharp transition between the efficient swimmers and the fast ones is also exhibited in figure 8 where the Strouhal number of the optimal swimmers of the Pareto front is plotted as a function of U^*. For $U^* = 1.23$, one can see an abrupt transition from St = 0.30 to 0.22. These values of the Strouhal number are typical of fish swimming at large Reynolds number with aspect ratios around AR = 6 (see Eloy 2012). In the next section, the variation of the Strouhal number of the most efficient swimmers with
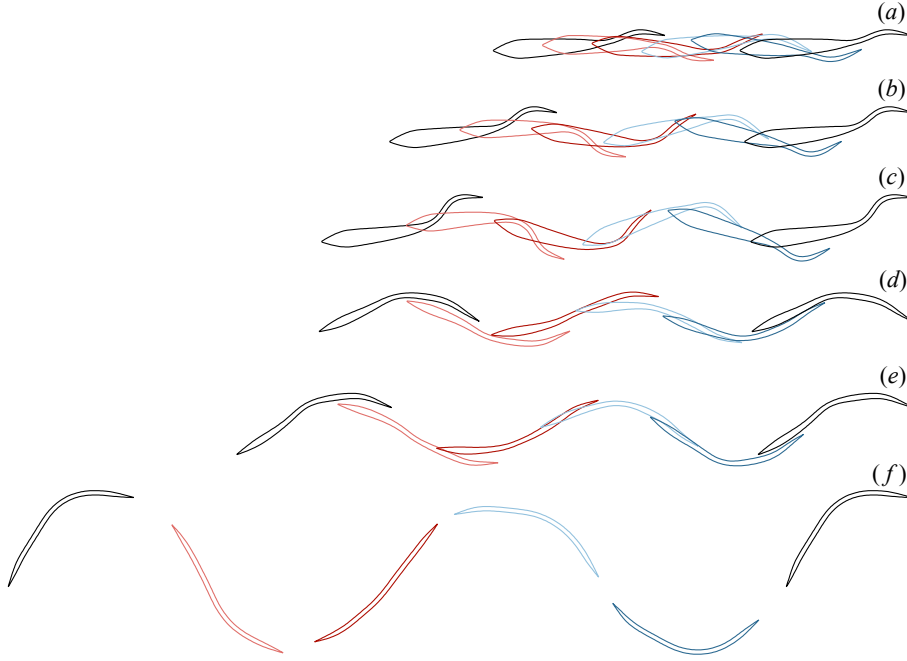
FIGURE 7. Swimming kinematics of the optimal swimmers as seen from above in the laboratory frame. Two periods are represented on each line $(a-f)$ and the labels are the same as in figures 5 and 6.
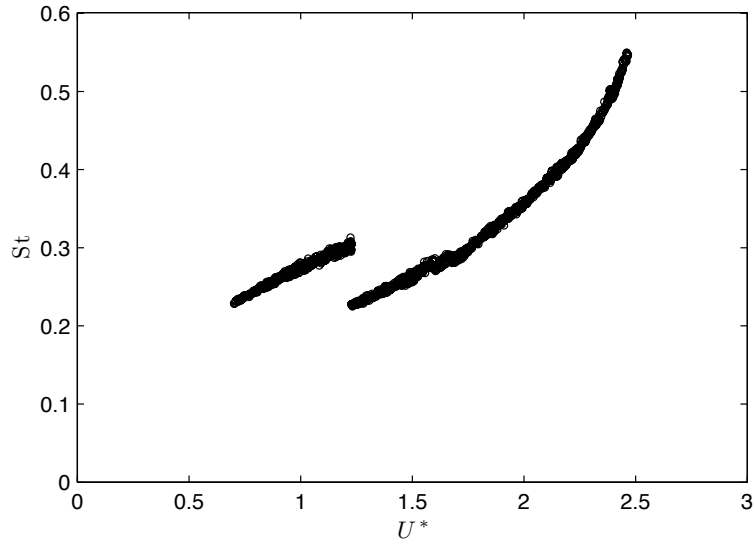

FIGURE 8. Strouhal number of the optimal swimmers as a function of U^*. The swimmers are the same as in figure 5.

the Reynolds number will be considered, and compared to the values measured on real animals.

The abrupt transition at $U^* = 1.23$ is also present when one examines how the different components of the energetic costs are distributed for each optimal swimmer, and how
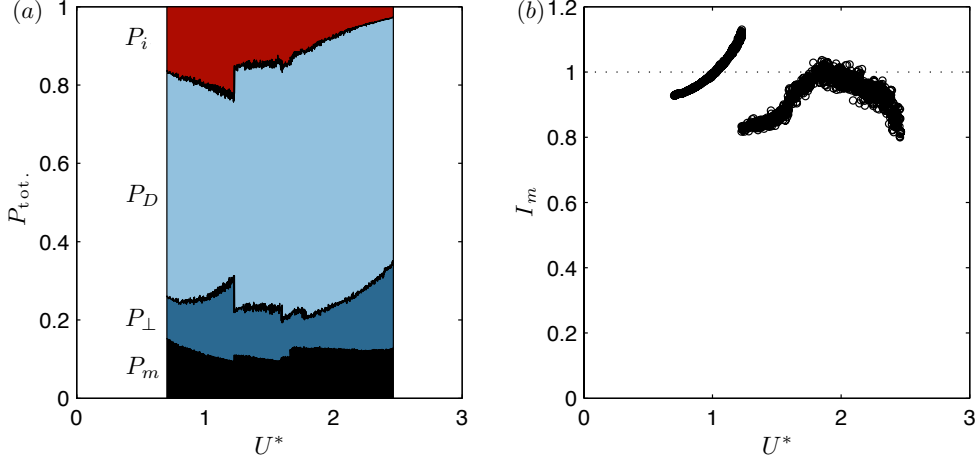
FIGURE 9. (a) Repartition of the lost power for the optimal swimmers as a function of U^*. The different powers are defined in (2.36): P_m is the reactive term and correspond to the energy lost in the wake, $P_\perp$ corresponds to the energy of the lateral drag forces, P_D is the power spent to balance the drag forces, both the form and the skin-friction drags, and P_i is the internal power loss due to the viscosity of the swimmer material. (b) Relative contribution of the reactive forces to the thrust. When $I_m > 1$, the resistive force actually produce a drag, i.e. a force in the $+x$ direction.

the reactive and resistive forces contribute to the total thrust (figure 9). Examining the repartition of energy losses in figure 9a, it can be noted that most of the energy is spent through the work of the drag forces. This amounts for more than 50% of the energetic costs for all optimal swimmers. The components P_m and $P_\perp$, corresponding respectively to the energy lost in the wake (the "reactive" energy) and to the work of the lateral drag forces, each amounts for approximately 10% of the energetic costs. Finally, the internal dissipation due to the viscoelastic nature of the fish material is of the order of 20% of the total energetic cost, but varies substantially along the Pareto front. For the efficient swimmers in the first lobe of the Pareto front (for $0.7 < U^* < 1.23$), the contribution of the internal dissipation increases with the stride length, as the amplitude of motion also increases. On the contrary, for the elongated swimmers of the second lobe of the Pareto front (for $1.23 < U^* < 2.5$), the contribution of the internal dissipation decreases with the stride length. This is due to the fact that, as the amplitude of the motion increases (which would contribute to an increase of internal dissipation alone), the shape become more and more slender, reducing the second moment of inertia I, as given by (2.7), and thus the energy dissipated internally, as given by (2.29).

In figure 9b, the contribution of the reactive force to the production of thrust is plotted for the different optimal swimmers. It can be seen that this contribution is always greater than 80% showing that the thrust is mainly achieved by the reactive forces, i.e. the added-mass effects. Surprisingly, this is also true for the fast swimmers of the second lobe of the Pareto front (for $1.23 < U^* < 2.5$), despite their slenderness.

To complete this study of the reference case, optimisation calculations have been performed where the shape of the swimmer was frozen and only the motion was allowed to vary (figure 10). Three frozen shapes (pictured in figures 6b, 6e, and 6f) have been used, corresponding respectively to an efficient swimmer, a moderately fast swimmer, and a very fast swimmer on the Pareto front. Each of these three frozen shapes leads to a different Pareto front, which, when put together, give an excellent approximation of the actual Pareto front (figure 10). This shows again that the Pareto front can be divided
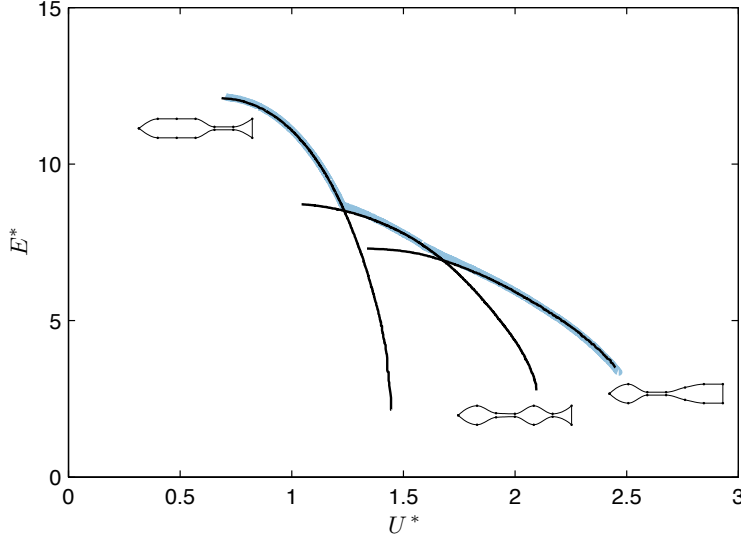
FIGURE 10. The Pareto front can be reproduced by using only three distinct "species". Each black line has been obtained with the evolutionary algorithm by freezing the shape functions, $a(s)$ and $b(s)$, such that they correspond to the optima of figures 6b, 6e, and 6f. The thick blue (grey) line correspond to the result of the optimisation when the shape is varied, as in figure 5, and is displayed for reference.

into two species: the efficient swimmers, and the fast swimmers (which can further be subdivided into two different shapes).

The unusual shapes and swimming gaits of the fastest swimmers raise the question of the model validity in this case. First, it is observed that, as the stride length U^* increases, so does the amplitude of the swimming path (figure 7d–f), reaching angles where the weakly nonlinear approximation adopted in the present paper is not valid anymore (for say $U^* > 2$). In addition, the contracting region observed after the "head" of these swimmers (figure 6d–f) may promote vorticity shedding that is not taken into account in the present model (this point will be discussed again in §6). Finally, these surprising swimming gaits, with large stride lengths U^*, may require unfeasibly large amounts of internal power, and this could explain why they seem so "unnatural". For these high-speed swimmer, the validity of the present model is therefore questionable. Specific experiments or numerical simulations would help to understand the particularity of the swimming hydrodynamics in this limit, and to refine the present approach. However, these limitations only concern the fastest "species" and not the efficient one that will be examined in more details in the following.

4.2. *Variation of the Reynolds number*

Different parametric studies have been carried out in which all the physical parameters of the reference case were kept constant except one that was varied. Discussions about the effect of a variation of the number of degrees of freedom, of the aspect ratio, or of the internal viscosity are deferred to the appendices A, B, and C. In the present section, the variation of the characteristics of the most efficient swimmer when the Reynolds number is varied from 10^4 to 10^6 are reported. As shown in figure 11, the swimmers with larger Re outperform the swimmers with smaller Re, but the Pareto front always exhibits the same property of having two lobes corresponding to efficient swimmers for the smaller U^* and elongated swimmers for larger U^*.
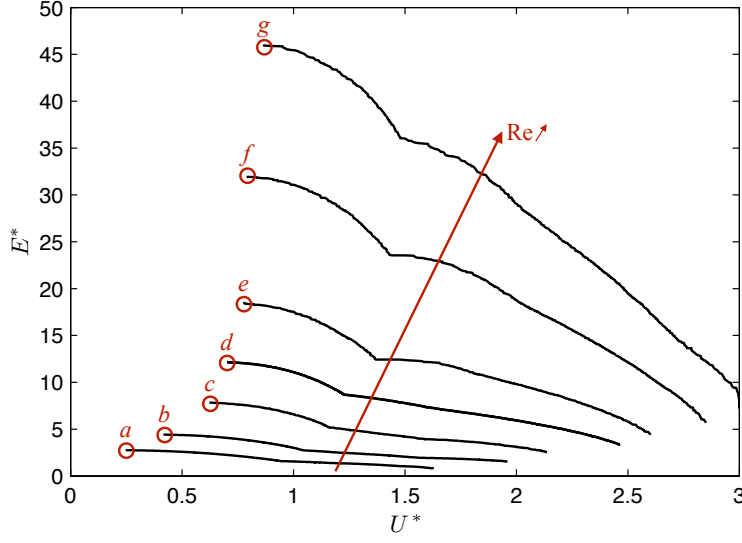
FIGURE 11. Results of the optimisation for different Re varying from 10^4 to 10^6. The circles and the attached labels correspond to the most efficient swimmers in each case. These particular swimmers are pictured in figure 12 and their characteristics are reported in table 4.
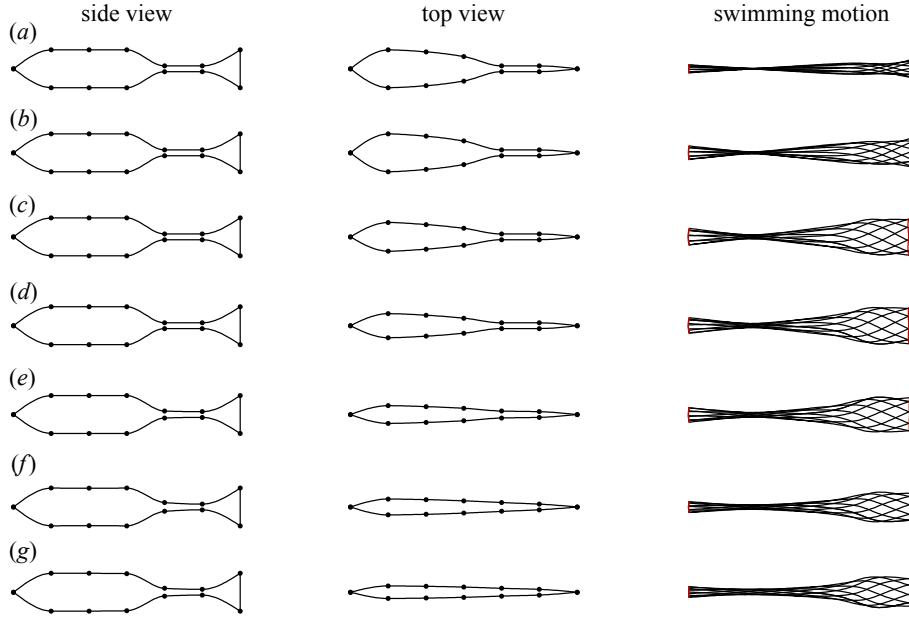

FIGURE 12. Geometry and kinematics of the most efficient swimmers when the Reynolds number is varied: (*a*) Re $= 10^4$; (*b*) Re $= 2 \times 10^4$; (*c*) Re $= 5 \times 10^4$; (*d*) Re $= 10^5$; (*e*) Re $= 2 \times 10^5$; (*f*) Re $= 5 \times 10^5$; (*g*) Re $= 10^6$. The characteristics and performances of these swimmers are reported in table 4.

The focus has been placed on the most efficient swimmer of the Pareto front for two reasons. First, this swimmer is representative of the whole first lobe of the Pareto front since the rest of this lobe roughly corresponds to the same swimmer with increased swimming amplitude, as it has been discussed above for the reference case. Second, it can be argued that, since the swimmer is free to change its beating frequency, a large

Reynolds number	Re	10^4	2×10^4	5×10^4	10^5	2×10^5	5×10^5	10^6
Figure		$12a$	$12b$	$12c$	$12d$	$12e$	$12f$	$12g$
Results	E^*	2.763	4.425	7.854	12.150	18.465	31.930	45.999
	U^*	0.248	0.417	0.623	0.702	0.774	0.790	0.864
	St	0.332	0.304	0.263	0.229	0.194	0.157	0.145
	Li	0.414	0.309	0.175	0.117	0.073	0.045	0.029
	$\theta_{\max}$	0.305	0.424	0.490	0.462	0.421	0.353	0.354
	U/V	0.309	0.467	0.591	0.632	0.676	0.707	0.750
	V_0	1.337	1.316	0.990	0.852	0.669	0.635	0.516
	I_p	0.179	0.230	0.212	0.220	0.163	0.187	0.186
	I_D	2.667	2.832	2.787	2.751	2.511	2.422	2.355
	I_w	1.679	1.609	1.651	1.623	1.689	1.594	1.563
	L/B	6.003	6.004	7.900	9.443	12.777	14.293	18.053
	S^*	1.584	1.517	1.374	1.363	1.145	1.008	1.057
	I_m	0.949	0.915	0.915	0.928	0.940	0.951	0.968

TABLE 4. Results of the parametric study when Re is varied from 10^4 to 10^6. The other parameters are the same as in the reference case: AR = 6, $N = 6$, $\mu_i = 10^4$ Pa s.

swimming speed U does not necessarily correspond to a large dimensionless velocity U^*, but can be achieved by keeping the energetic efficiency E^* maximum while increasing the frequency. Strictly speaking, for an animal of given length, the swimming speed cannot be increased without also increasing the Reynolds number and thus changing the constraints on the optimisation. But, since the characteristics of the most efficient swimmers do not qualitatively change with the Reynolds number as it will shown below, it is true to say that, for a given efficient swimmer, increasing its undulatory frequency without changing the swimming amplitude will lead to larger swimming speed with still near-optimal efficiency. Thus achieving a large efficiency E^* seems more important than achieving a large stride length U^*. In reality, the efficiency of fish muscles depends on frequency and amplitude such that increasing U^* can be beneficial, but it is beyond the scope of the present paper to take these frequency and amplitude dependencies into account.

The variation of the performances of the most efficient swimmer as Re is varied will be discussed in more detail below when comparing with biological data on aquatic animals. In particular, the variation of U^*, E^*, St, and $\theta_{\max}$ with the size of the swimmer will be examined. The striking feature of the different shapes reported in figure 12 is that the width and the volume of the most efficient swimmer strongly depend on the Reynolds number. For Re $\leqslant 2 \times 10^4$, the maximum width B reaches the upper bound imposed by the constrains such that the thickness aspect ratio is $L/B \approx$ AR = 6, but as Re increases, this value increases too to reach $L/B \approx 18$ for Re $= 10^6$. This is accompanied by a decrease of the volume as reported in table 4.

This qualitative change in the swimmer shape can be explained by comparing two swimmers with different Reynolds numbers. For the smallest Reynolds numbers, the reactive thrust force has to be comparatively larger to compensate a larger skin-friction drag (in dimensionless units). But this larger thrust force goes with a larger periodic torque exerted on the body as the thrust is mainly produced by the posterior section and has a non zero normal component at each instant. To avoid a large recoil pitching motion in this case, the inertia of the anterior region thus needs to be larger, explaining why the volume and the width are larger for the smallest Reynolds number.

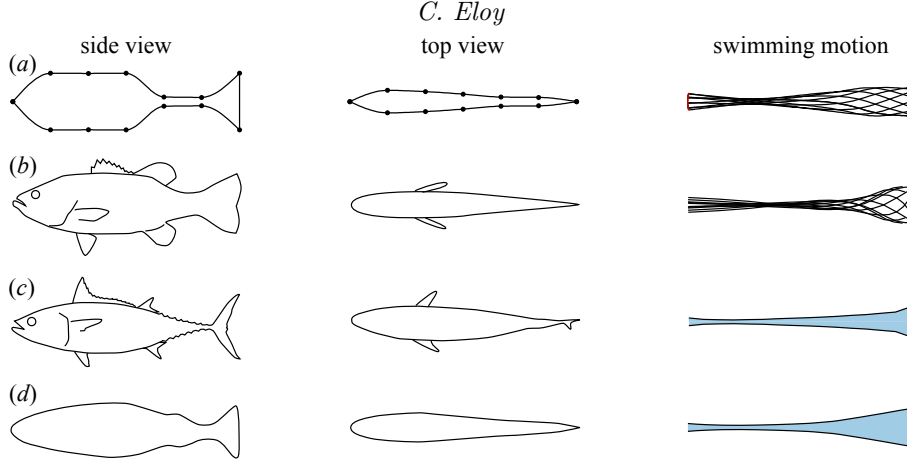It is interesting to note that this increase in thickness for the smallest Reynolds number

FIGURE 13. Geometry and kinematics of the most efficient swimmer when AR = 4 (*a*) compared to different species of fish: Largemouth bass (*Micropterus salmoides*) (Jayne & Lauder 1995) (*b*); Kawakawa tuna (*Euthynnus affinis*) (Donley & Dickson 2000) (*c*); Saithe (*Pollachius virens*) (Hess & Videler 1984) (*d*). The most efficient swimmer in (*a*) is the same as in figure 23*a*. The blue (grey) shaded region in the last column corresponds to the envelope of the deformation. The characteristics and performances of these swimmers are reported in table 5.

is accompanied by a larger drag coefficients. Indeed, the coefficients I_D, I_w, and S^* are decreasing function of Re (table 4), except when Re $= 10^4$ for which the swimming amplitude is much smaller. In other words, the optimal shape is achieved by balancing drag reduction and inertia, and this balance is strongly dependent on the Reynolds number.

In the appendices A, B, and C, additional parametric studies are reported where the number of degrees of freedom, the aspect ratio, and the internal viscosity have been varied. These different parametric studies show that the main characteristics of the optimisation results are robust to any change of the physical parameters. In particular, the existence of two 'species' on the Pareto front, one specialised in efficient swimming, the other in fast swimming, is always recovered in the optimisation calculations. In the next section, a comparison with experimental observations on aquatic animals will be drawn.

5. Comparison with aquatic animals

To begin the comparison with aquatic animals, the morphologies and the performances of different species of fish are compared with one result of the present optimisation calculations in figure 13 and table 5. Three species of fish have been chosen, a bass (Jayne & Lauder 1995), a tuna (Donley & Dickson 2000), and a saithe (Hess & Videler 1984), swimming at a Reynolds number Re $\approx 10^5$ and with an aspect ratio AR ≈ 4. They are compared to the most efficient swimmer found in the case of an aspect ratio AR = 4, with Re $= 10^5$ (Appendix B).

The morphology of the model and of the real fish are very similar. Although the thickness ratio L/B is slightly higher in the model, the top views in figure 13 reveal almost identical streamlined shapes. The side views all exhibit a large anterior region, a caudal peduncle of reduced cross-section, and a tail of similar depth as the maximum depth of the anterior region. The swimming characteristics of the different species of fish are also very similar to the characteristics of the most efficient swimmer (table 5). In particular, their stride length U^* and slip ratio U/V are almost the same, while the

Species		model	bass	tuna	saithe
Aspect ratio	AR	4	3.8	3.5	4.1
Reynolds number	Re	10^5	1.4×10^5	1.8×10^5	3.9×10^5
Figure		$13a$	$13b$	$13c$	$13d$
Results	U^*	0.751	0.591	0.595	0.794
	St	0.171	0.223	0.212	0.230
	U/V	0.670	0.739	0.613	0.757
	L/B	10.051	8	6.5	7.9

TABLE 5. Comparison of the characteristics and performances of the most efficient swimmer when AR = 4 and different species of fish.

Strouhal number is about 30% larger for real fish. This difference is probably due to the non-actuated nature of the caudal fin for most animals as is explained below.

It should be noted that, in the case of the tuna (figure $13c$), the lunate shape of the tail can significantly improve the production of thrust (Chopra & Kambe 1977). Although this effect cannot be captured within the present elongated-body approximation, the results for the tuna reproduced in table 5 agree reasonably well with the characteristics of the most efficient swimmer predicted by the optimisation calculation.

The comparison of the present results with aquatic animals is further explored by examining the evolution of the swimming performances as the Reynolds number is varied. In a previous paper, kinematic data on swimming animals have been compiled and compared to an inviscid optimisation calculation (Eloy 2012). These biological data correspond to an almost exhaustive review of the literature on the subject and comprise 66 independent measurements on 53 different species. They have been divided into 7 groups for convenience: 8 different species of mammals, 4 of sharks, 8 of scombrids (a family including tunas, bonitos and mackerels), 11 of fish from the orders of Perciformes and Salmoniformes, 19 of fish from other families (including the orders of Cypriniformes, Gadiformes and Mugiliformes), 10 of 'elongated' fish (including eels, needlefish of the family of Belonidae, and other fish with large aspect ratios) and 6 species categorised as 'others' gathering one reptile (crocodile), two frog tadpoles, two amphibians (axolotl and siren) and one annelid (leech).

The optimisation carried out in Eloy (2012) was done using Lighthill's large-amplitude elongated-body theory (Lighthill 1971), for which the thrust and the kinetic energy lost in the wake are functions of the tail kinematics only. This remarkable property allowed to optimise the motion of the tail for a given thrust, i.e. to minimise the energy lost in the wake when the thrust balances a given drag on average. In the present paper, resistive forces are taken into account in addition to reactive forces, and the whole kinematics of the body is included in the analysis through the recoil motions and the modification of the skin-friction drag by the motion.

5.1. *Kinematics*

In figure 14, the optimal Strouhal number predicted by the inviscid analysis is compared to the present results and to measurements on the different swimming animals. In the inviscid analysis of Eloy (2012), the optimal Strouhal number St was only a function of the Lighthill number, Li, which is defined in (2.38). In the present optimisation calculation, St also depends on the different physical parameters of the problem: the aspect ratio, the internal dissipation, and the number of degrees of freedom, but it appeared that the
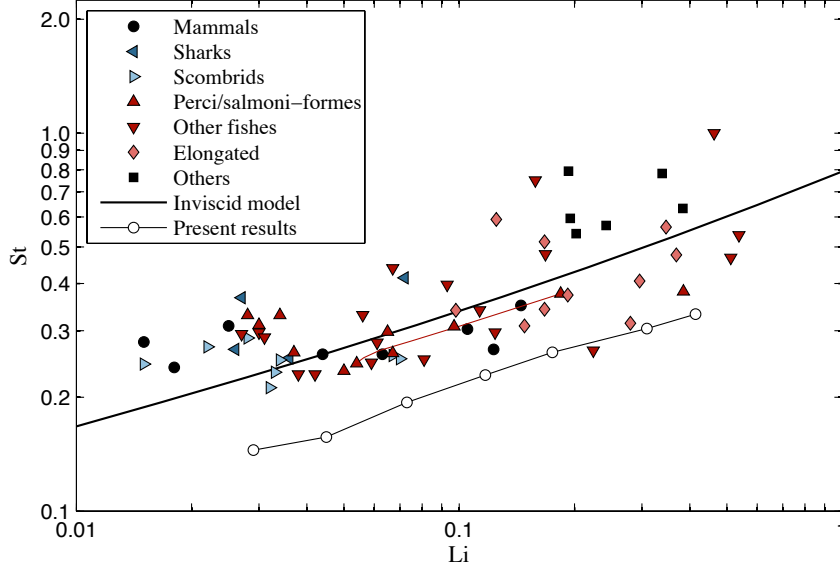
FIGURE 14. Strouhal number St as a function of the Lighthill number Li. The different symbols represent different groups of animals compiled in Eloy (2012), as reported in the legend. The thick solid line is the prediction of an inviscid optimisation based on the elongated-body theory of Lighthill (1971). The open circles correspond to the data of the present paper, when Re is varied between 10^4 and 10^6 (Li is roughly proportional to $Re^{-1/2}$), reported in table 4 and figure 12.

variation of the Reynolds number is the major effect in the parametric studies reported above and in the Appendices.

Figure 14 shows that the most efficient swimmers predicted in the analysis exhibit Strouhal numbers that are increasing with the Lighthill number. The scaling of this dependency is similar to the results of the inviscid optimisation, roughly $St \sim Li^{1/3}$, and a comparable trend also appears in the biological data, although the important scatter in that case does not allow one to estimate the precise scaling law. However the optimal Strouhal number in the present case is always lower than the prediction of the inviscid analysis and than the biological data. This can be explained by the following arguments. When compared to the inviscid analysis, the present calculations include two additional sources of energy loss: the internal dissipation, and the 'resistive energy loss' due to transverse drag forces (figure 9a), both of which increase when the amplitude of the swimming motion increases. This explains why the optimal amplitude and the Strouhal number are lower when these effects are taken into account: in other words, it is advantageous to decrease the swimming amplitude because the increased reactive energy loss is compensated by smaller energy losses both internally and resistively.

One question remains however: why are the Strouhal numbers observed on real animals systematically larger than in the present optimisation calculations? One reason could be that the biological data are obtained by averaging over a large number of observed kinematics, most of them being not optimal. This could induce a statistical bias, which, added to a possible underestimate of the drag on swimming fish, would tend to overestimate the Strouhal number for a given Lighthill number. Another source of the discrepancy could be the model approximations. The underestimate of the Strouhal number could be a sign of an overestimate of the thrust force or an underestimate of the drag by the model. Finally, an additional reason for this discrepancy could be that swimming animals
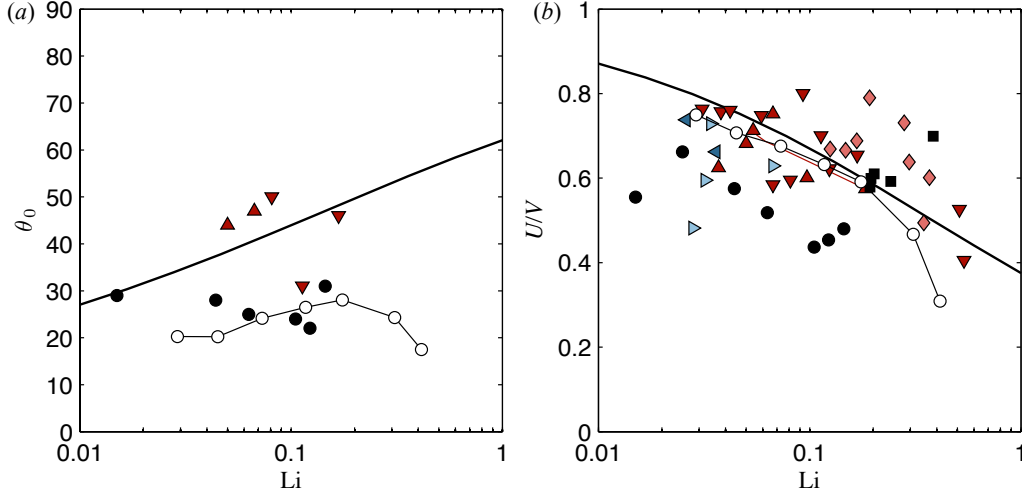
FIGURE 15. Variation of the maximum incidence angle of the tail (*a*) and the slip ratio (*b*) as a function of the Lighthill number. The legend is the same as in figure 14.

have generally a passive caudal fin, which results in swimming gait envelopes that are qualitatively different from the present calculations. As seen in figure 6*a* for instance, the present optimisation analyses always predict that the most efficient swimmers beat their tail such that the maximum excursions correspond to a zero incidence angle. In other words, the width of the swimming mode envelope is constant near the tail. The same prediction can be reached with an inviscid analysis in the linear (Lighthill 1971) or the weakly nonlinar limit (Eloy 2012). In contrast, fish usually exhibit a widening of the envelope near the tail (e.g. Lauder & Tytell 2005) as shown in figure 13*c* and 13*d* for instance. This widening is likely due to the non-actuated nature of the tail. This difference may not drastically change the performance of swimming but will affect the measure of the tail beating amplitude and therefore the Strouhal number.

In figure 15, two other characteristics of the swimming kinematics, the maximal incidence angle at the tail θ_{max} and the slip ratio U/V, are plotted as a function of the Lighthill number for the present optimisation calculations, the inviscid analysis, and the aquatic animals. In coherence with the results on the Strouhal number, the incidence angle at the tail is lower in the present simulations than in the inviscid analysis of Eloy (2012). The reason for this discrepancy is the same as the one evoked above: the additional dissipative terms favour lower amplitude in the present optimisation. The maximum incident angle at the tail has been measured only in few experiments and therefore the comparison with biological data is delicate. However, the typical angles observed for mammals, $\theta_{max} \approx 25°$, are similar to the ones of the most efficient swimmers in the present analysis, and the values measured on fish species $\theta_{max} \approx 45°$ are closer to the results of the inviscid analysis (figure 15*a*).

The slip ratio U/V has been more widely measured in the literature as seen in figure 15*b*. However, some care should be taken when analysing these data as the method used to measure the wave speed V may have a strong influence on the results as already noted by Webb *et al.* (1984). To illustrate this effect, the amplitude and phase of the curvature, the incident angle, and the y-position are plotted in figure 16 as a function of the position on the backbone. Through figure 16*b*, it appears clearly that the wave speed, which is proportional to the slope of the phase angle (more precisely a wave speed V can be defined for any phase $\phi(s)$ as $V = -\omega \, ds/d\phi$), varies along s and is different for the
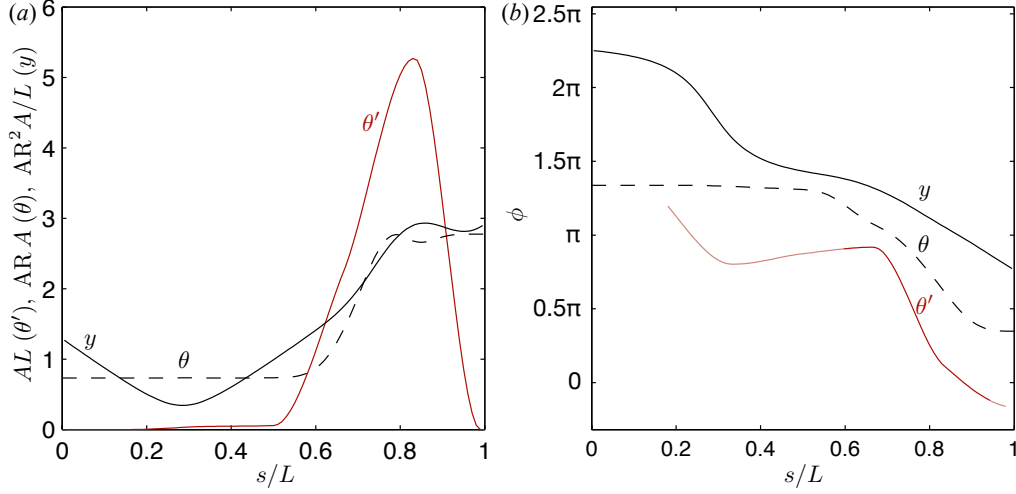
FIGURE 16. Illustration of the amplitude (*a*) and phase (*b*) of the curvature θ' (solid red/grey line), the incident angle θ (dashed line), and the excursion y (solid black line) as a function of the curvilinear coordinate s/L. The kinematics chosen in this example corresponds to the most efficient swimmer in the reference case (figure 6*a*). These three functions can be written as $f(s,t) = A(s)\mathrm{e}^{\mathrm{i}\phi(s)}\mathrm{e}^{\mathrm{i}\omega t}$, where A is the amplitude and ϕ the phase. The amplitudes are normalised by $1/L$, $1/\mathrm{AR}$ and L/AR^2 respectively (*a*). The phase of θ' is plotted only when the corresponding amplitude is non zero and appears shaded when the amplitude is lower than 5% of its maximum.

three different functions. In the present paper, the wave speed has been defined in (2.39) to be the average wave speed of y on the last 10% of the body. In the experimental data on swimming, the wave speed is sometimes evaluated with a similar method (a longer part of the body is usually used however), some other times the curvature is used, or an estimate of the wavelength of the deformation is used together with the tailbeat frequency. It is thus not surprising that the data on swimming animals appear quite scattered in figure 15*b*. Nevertheless, when one examine each animal group independently (except for sharks), a clear tendency emerges: the slip ratio U/V is a decreasing function of Li, as was predicted by the inviscid analysis, and as is observed in the present optimisation calculations. The order of magnitude of the slip ratio is also similar in the three cases: $U/V \approx 0.6$.

In figure 17, the stride lengths of the different swimming animals reported in the literature are compared to the stride lengths of the most efficient swimmers (the results of the inviscid analysis do no appear on this figure because the optimisation does not depend on the stride length in this case). It should first be noted that the stride length of the most efficient swimmer (i.e. the one maximising E^* in figure 5, for instance) is not highly constrained since a slight change in E^* on the Pareto front can lead to important modification of U^*. Nevertheless, the agreement between the predicted U^* and the measured one is very good (figure 17). In particular, one can observe that the stride length is a decreasing function of the Lighthill number, or equivalently an increasing function of the Reynolds number. This result contrasts with the generally accepted assumption that the stride length is fairly constant and equal to $U^* \approx 0.65$ for all fish (Videler 1993).

5.2. *Energetics*

In figure 18, a comparison of the efficiency of the most efficient swimmers with experimentally measured values is carried out. The experiments reported in this figure are
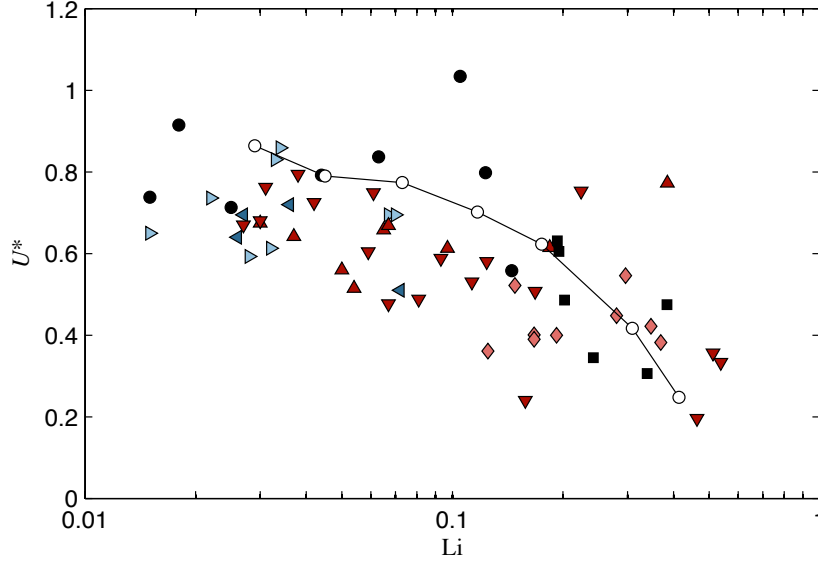
FIGURE 17. Stride length U^* as a function of the Lightill number Li for the most efficient swimmers (solid line and open circles) and for different aquatic animals (filled symbols with the same legend as in figure 14).
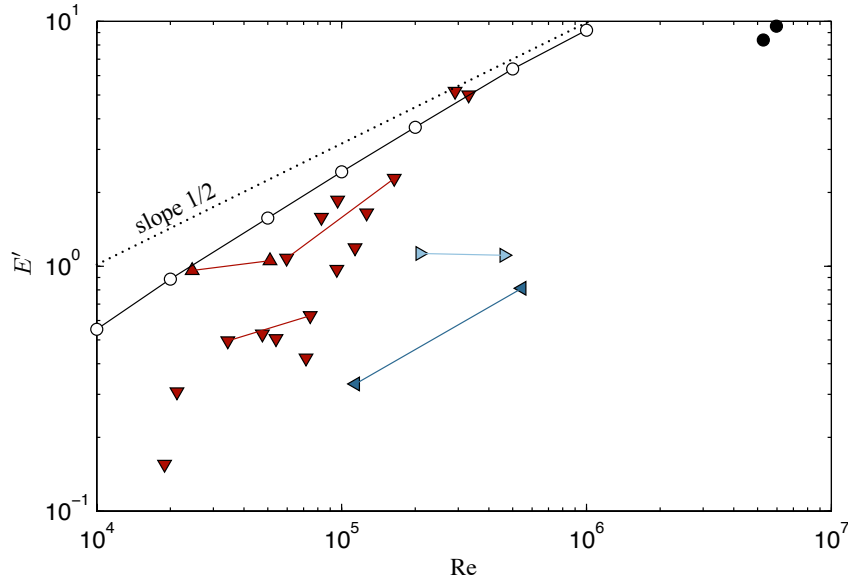

FIGURE 18. The total efficiency E' of different aquatic species is compared to the results of the present analysis when the Reynolds number is varied. The total efficiency is defined in a similar manner as E^*, given by (2.32), except that the total metabolic rate is used as the power cost, such that $E' = \rho Vol^{2/3} U^3 / P_{\mathrm{MR}}$, with P_{MR} the total metabolic rate. The relation $P_{\mathrm{MR}} = 5 P_{\mathrm{tot.}}$ has been assumed to plot the present results (see the main text for a justification of this factor).

the same as the ones used by Videler (1993) when he discussed the 'cost of transport' (COT) of different animals. The total efficiency, $E' = E^*/5$, used in the present study is similar to the inverse of the COT, except that the acceleration $U^2/Vol^{1/3}$ has been used instead of gravity to make the efficiency dimensionless. The other difference is that

COT and E' are based on the total metabolic rate of the animals, which includes the heat produced in the muscles and the metabolic rate used for other tasks than swimming (such as the functions of the heart, the brain, the digestive organs, etc.). To estimate the ratio between the total efficiency E' and the 'mechanical' efficiency E^*, it has been assumed that muscles have an efficiency of 50%, as reported in Curtin & Woledge (1993), which is probably an upper bound, and that only 40% of the metabolic rate is devoted to swimming as proposed by Weihs (1973) based on a simple optimisation calculation. When combined, these rough estimates explain the tentative factor 5 between E^* and E'.

Figure 18 shows that the total efficiencies of the present model are in good quantitative agreement with the experimental data. It can further be noted that the predictions represent an upper bound for the experimental data. This is consistent with a possibility of an overestimate of the muscle efficiency and it is also consistent with the fact that predictions correspond to the maximum possible E'. One can also observe in figure 18 that E' increases with a slope that is larger than the naive scaling law $E' \sim \mathrm{Re}^{1/2}$ that would be obtained if the metabolic rate was proportional to a laminar drag coefficient $C_D \sim \mathrm{Re}^{-1/2}$. The slope is actually close to $E' \sim \mathrm{Re}^{0.6}$. The reasons of this larger slope likely originate from the following observation: as the Reynolds number increases, both the recoil motions and the internal dissipation reduce, which yields better streamlining, smaller drag coefficients and better conversion of energy into thrust.

The comparison of the performances of the most efficient swimmers with aquatic animals have shown remarkable similarities. Most of the characteristics of the salmon-like fish, which gather the sub-carangiform, carangiform, and thunniform subclasses (as explained in § 1) are recovered in the present analysis. The only difference is the Strouhal number which is systematically larger for real animals than in the present simulations. This difference could be due to either statistical biases in the experimental measurements, invalid approximations of the present model, or to the inherent non-actuated nature of caudal fins in most animals.

5.3. *Large aspect ratio swimmers*

Let us now examine the particular case of very elongated swimmers. To address this point, additional calculations have been performed for swimmers of aspect ratios AR = 15, and with a moderately low internal viscosity, $\mu_i = 10^3 \, \mathrm{Pa\,s}$, as illustrated in figure 19 and table 6. Two optimisations have been carried out, one where the shape of the swimmer was free to vary, and another one where an eel-like shape was assumed and only the motion was optimised. The most efficient swimmers in both cases are compared to two species of elongated fish, the American eel (Gillis 1998; Tytell & Lauder 2004) and the hagfish (Long *et al.* 2002), which share similar aspect ratios and Reynolds number.

First, it should be noted that the swimming kinematics of the American eel as reported by Gillis (1998) does no exhibit large curvatures all along the backbone (figure 19*c*) as it would be expected from an anguilliform swimmer and is, in fact, very similar to the kinematics of the salmon-like bass (Jayne & Lauder 1995) shown in figure 13*b*. According to the experimental results of D'Août & Aerts (1999) and Ellerby *et al.* (2001), the swimming mode envelope of eels can change depending on the swimming velocity, which indicates that eels can likely switch from a salmon-like kinematics with the large curvatures localised in the posterior region for small swimming velocities to an anguilliform kinematics without such a localisation for large swimming velocities. An example of the latter kinematics is shown in figure 19*d* for the hagfish (Long *et al.* 2002).

Examining the results of the optimisation calculation, it can be seen that the most efficient swimmers display two different kinematics whether the shape is constrained to

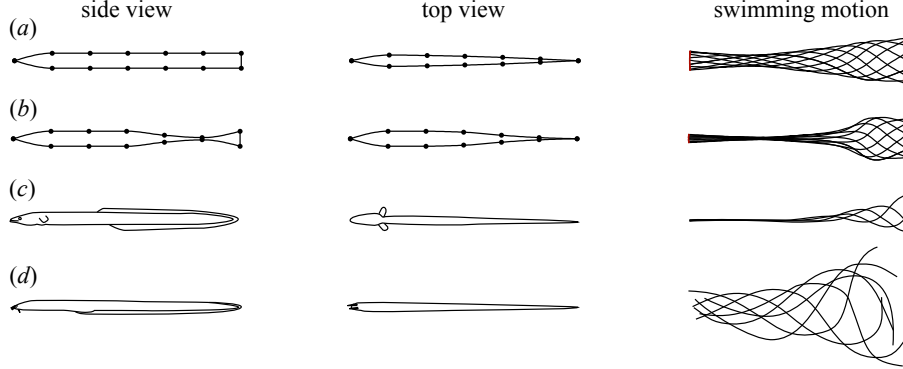| side view	top view	swimming motion

FIGURE 19. Geometry and kinematics of very elongated swimmers. The parameters of the optimisation are the same as in the reference case except that the internal viscosity is $\mu_i = 10^3 \,\mathrm{Pa\,s}$ and the aspect ratio AR $= 15$. The first row (a) correspond to the most efficient kinematics when the optimisation is performed with a frozen eel-like shape as pictured in the first two columns. The second row (b) is the most efficient swimmer obtained by optimising both the shape and the motion as in the rest of this paper. The two bottom rows correspond to biological data: American eel (*Anguilla rostrata*) (Gillis 1998) (c) and Hagfish (*Myxine glutinosa*) (Long *et al.* 2002) (d) The characteristics and performances of these swimmers are reported in table 6.

Species		model (eel)	model (free)	eel	hagfish
Aspect ratio	AR	15	15	11	17
Reynolds number	Re	10^5	10^5	6×10^4	6.4×10^4
Figure		19a	19b	19c	19d
Results	E^*	7.193	9.755	—	—
	U^*	0.631	0.482	0.448	0.422
	St	0.317	0.365	0.314	0.564
	$\theta_{\max}$	0.541	0.619	0.8	1.5
	U/V	0.565	0.520	0.731	0.494
	L/B	20.000	15.000	20	24
	I_m	0.645	0.709	—	—

TABLE 6. Comparison between the characteristics of the most efficient swimmers of aspect ratio AR $= 15$ and internal viscosity $\mu_i = 10^3 \,\mathrm{Pa\,s}$ (one constrained to have an eel-like shape, the other not), and two species of anguilliform fish, the American eel (Tytell & Lauder 2004) and the hagfish (Long *et al.* 2002).

be eel-like or not (figure 19a,b). These two swimming modes are visually similar to the two different kinematics observed on real elongated swimmers (figure 19c,d) and their characteristics compare reasonably well, at least qualitatively (table 6). The difference in kinematics when the shape is eel-like or not is likely due to the presence of a caudal peduncle. When it is present, the extra cost of having a steep increase of the envelope amplitude is decreased; without it, one expects a smoother envelope. Note that, in both cases, the major part of the thrust still originates from the reactive forces (I_m in table 6), in agreement with the numerical simulations of Tytell *et al.* (2010) on eel-like swimmers using a Navier–Stokes solver. Note also that the efficiency in the 'free-shape' case is $E^* = 9.8$, which is much smaller than the result $E^* = 16.2$ obtained for an aspect ratio AR $= 6$ and same internal viscosity $\mu_i = 10^3 \,\mathrm{Pa\,s}$ (Appendix C). However, the volume of the elongated swimmer is also much smaller, and if one was to compare optima of similar volumes, the corresponding Reynolds number for AR $= 6$ would be Re $\approx 5 \times 10^4$ and

the efficiency would then drop to $E^* \approx 10.7$ if one follows the scaling law $E^* \sim \mathrm{Re}^{0.6}$ found in §5. Therefore, when this volume effect is taken into account, the efficiency of the most efficient swimmers is almost constant as the aspect ratio is varied, and, as a consequence, the penalisation in terms of efficiency of having a very elongated body is not large.

6. Discussion

In this paper, a hydrodynamical model of swimming animals has been proposed based on the elongated-body theory of Lighthill (1971) and extended to take into account some important viscous effects. This proposed model includes reactive forces, resistive forces, and the modification of the drag by the swimming motion. It is nonlinear and valid up to the first nonlinear corrections. It also takes into account the dissipative viscoelastic nature of the soft tissues. With this model, it has been shown that, when an animal is swimming steadily by bending its backbone periodically, the different Fourier components of Newton's second law can be used to calculate efficiently and rapidly the full kinematics and energetics of swimming.

The developed model has then been used to perform a bi-objective optimisation, where swimmers with large efficiencies, large velocities, or any trade-offs between the two were sought. This constrained bi-objective optimisation has been performed using an evolutionary algorithm tailored to this specific problem, where the shape and the motion of the swimmers are varied simultaneously. Interestingly, it has been found that the morphology of the optimal swimmers could be divided into two distinct species: the first species is reminiscent of tuna-like or salmon-like swimmers and is specialised in efficient swimming, the second species is more elongated and is specialised in fast swimming. It has further been shown that this division into two classes of swimmers is robust to any change of the numerical parameters (aspect ratio, number of degrees of freedom) or physical parameters (Reynolds number, internal viscosity of the soft tissues). Then, focusing on the efficient tuna-like species, it has been shown that its characteristics and performances compare remarkably well with most aquatic species reported in the literature, except for the Strouhal number that is generally larger for real fish than it is in the simulations.

The species of efficient swimmers found in the present simulations share the characteristics evoked by Lighthill (1970) and summarised in §1. Their morphologies show a large anterior region separated from the caudal fin by a caudal peduncle of reduced cross-section. The envelope of the swimming motion exhibits a minimal width over the anterior region, then displays a steep increase in the peduncle region, and finally is almost constant at the tail such that the tail incident angle is zero at the extrema of its motion. As already pointed out by Lighthill (1970), the recoil motion produced by the periodic torque exerted at the tail by the reactive forces is of major importance for this species. Because of the internal viscosity and the important thickness of the anterior region, the main body ahead of the peduncle remains almost rigid to avoid prohibitive viscoelastic costs, such that the only way for this species to prevent inefficient recoil motions is through inertia of the anterior region. This has interesting consequences on the optimal morphologies. For instance, the ratio of the animal length to its maximal thickness, L/B, is expected to be an increasing function of the Reynolds number as long as the boundary layers remain laminar.

The second species discovered in the optimisation calculations, the group of fast swimmers, is more elongated than the efficient swimmers and make use of a different mechanism to prevent unwanted recoil motions. These swimmers use bending to counterbalance the torque applied at the tail such that, when seen in the laboratory framework, they

seem to swim with their whole body following a sinusoidal path. To explore this point further, specific calculations have been carried out with very elongated swimmers. These calculations have shown that animals found in nature can be related to the most efficient swimmers calculated in the optimisation calculations, even when the aspect ratio is large. The second optimal species however, which is associated with large stride lengths, does not seem to be related to any known animal. This shows that evolution is consistent with the selection of high-efficiency swimmers. This can be understood by realising that, keeping their stride length constant but increasing their tailbeat frequency, animals can increase their swimming velocity.

The presence of a caudal peduncle for all the optimal swimmers calculated here raises an interesting question. When examining the exchange of reactive energy between the swimmer and the fluid, one finds that the average power given to the fluid at each cross-section is $\left[\frac{1}{2}m\langle w^2 u\rangle\right]'$, which, when integrated along the length of the swimmer, gives the total reactive power in (2.28). This expression can take negative values when m' is negative, or equivalently when the depth decreases with s as it is the case just ahead of the caudal peduncle. This means that these cross-sections receive, on average, energy from the outer flow. The question here is whether the fish can 'harvest' this kinetic energy of the fluid? If they cannot, then the presence of the peduncle may not be as beneficiary and could explain why elongated fish such as eels do not exhibit one. To answer this question, one would need to take into account the detailed internal mechanics of the swimmers and, in particular, how the bending energy couples with the other sources of energy, which is beyond the scope of the present study.

The presence or absence of a caudal peduncle is related to another important point of elongated-body theory. When the fish's depth decreases abruptly, as it is the case just ahead of the peduncle or when ventral or dorsal fins are present, vorticity can be shed. As formulated by Lighthill (1971), the nonlinear elongated-body theory does not take into account this vorticity shedding. Wu (1971*b*) developed an extension of Lighthill's theory to model this effect; however, his approach is only valid in the linear regime and is difficult to extend to the present nonlinear framework. To understand better the importance of these contracting regions, a fully viscous numerical simulations at high Reynolds number would be necessary.

As was already noted in §1, Tokić & Yue (2012) have recently published a study similar to the present one, where they also performed bi-objective optimisation calculations by varying both the shape and the motion of elongated swimmers. They chose similar performance variable: the swimming speed and the cost of transport (which is inversely proportional to the efficiency used here). Compared to their study, the present paper incorporates several important features such as resistive forces and the enhancement of skin-friction drag due to the swimming motion. Another important difference is that the present model is weakly nonlinear, which allows to predict the amplitude of the swimming motion from hydrodynamic arguments only. The number of degrees of freedom is also slightly larger here (22 instead of 9), which allows to consider more general swimming motion, whereas Tokić & Yue (2012) have limited their study to bending waves of constant phase velocity with wavelengths equal to one body length. To explain the saturated amplitude of the motion without resorting to nonlinear effects, Tokić & Yue (2012) introduced a model of muscle activity, which states that the available power at a given section is proportional to the cross-section area. It is noteworthy that, despite the numerous differences in the modelling, most of the conclusions are similar. In particular, they found that the morphology of salmon-like swimmers is favoured when the cost of transport is optimised. They also found that the large amplitudes of the swimming envelope are localised near the tail when efficiency is optimised, but not when swimming
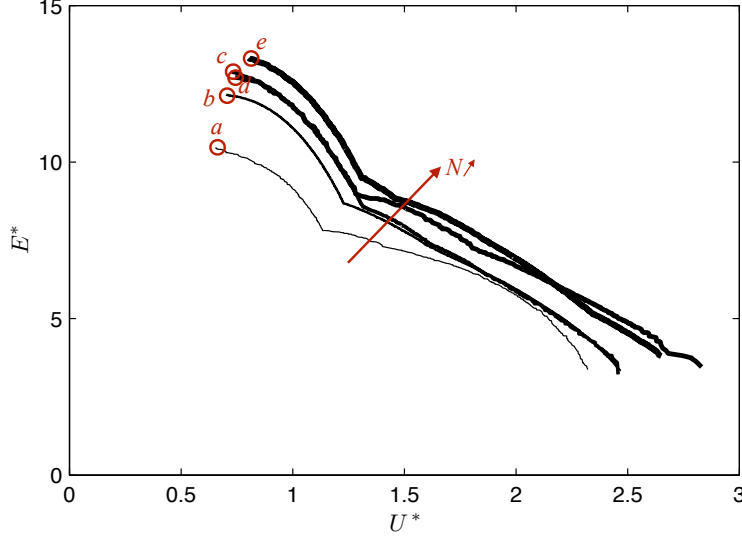
FIGURE 20. Results of the optimisation for different N varying from 5 to 9. The circles and the attached labels correspond to the most efficient swimmers in each case. These particular swimmers are pictured in figure 21 and their characteristics are reported in table 7.

velocity is maximised. However, they found that the thickness ratio, L/B, decreases with the animal size, while the opposite conclusion was reached here.

Appendix A. Variation of the number of degrees of freedom

The robustness of the numerical optimisation can be tested by varying the number of collocation points N between 5 and 9, the reference case corresponding to $N = 6$. The results of these calculations lead to very similar Pareto fronts as illustrated in figure 20. In particular, there are always two lobes corresponding to the efficient "species" and the fast "species" respectively. As expected, as N is increased and thus as the number of degrees of freedom is increased, the Pareto fronts obtained are generally better, i.e. the individuals on the Pareto front with the larger N dominate the individuals of lower N. There are few exceptions that may be due to insufficient convergence of the optimisation for the largest N or to the position of the collocation points.

As the figure 21 and table 7 show, the characteristics of the most efficient swimmer do not strongly depend on the number of collocation points N. In particular, the shape is always roughly the same: an anterior region of large depth with a maximum width B approximately equal to 10% of the length and a dimensionless volume $V_0 \approx 0.8$ (as defined by (2.4)), a thin cross-section spanning over 2 or 3 degrees of freedom and a flat tail of maximum span. The swimming motions are also very similar with the anterior region being rigid and the curvature being concentrated on the thinnest cross-sections.

This parametric study therefore shows that the results are robust to changes in the number of degrees of freedom. The value $N = 6$ chosen for the reference case gives results that are representative of what can be obtained with a larger number of degrees of freedom, with the advantageous property of converging faster.
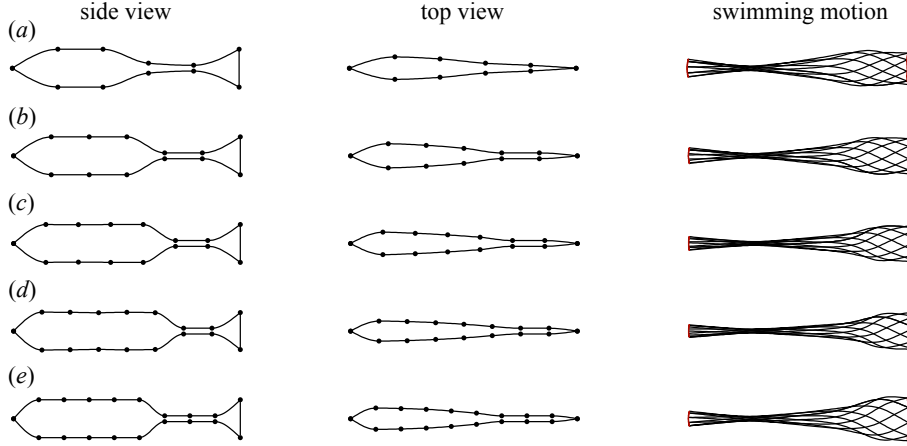
FIGURE 21. Geometry and kinematics of the most efficient swimmers when the number of degrees of freedom is varied. Each line (*a–f*) corresponds to a different value of N from 5 to 9. The characteristics and performances of these swimmers are reported in table 7. The different columns are the same as in figure 6.

Collocation points	N	5	6	7	8	9
Figure		21*a*	21*b*	21*c*	21*d*	21*e*
Results	E^*	10.447	12.150	12.872	12.700	13.324
	U^*	0.652	0.702	0.726	0.829	0.803
	St	0.220	0.229	0.221	0.221	0.243
	Li	0.109	0.117	0.114	0.114	0.116
	$\theta_{\max}$	0.449	0.462	0.437	0.436	0.513
	U/V	0.645	0.632	0.631	0.630	0.651
	V_0	0.734	0.852	0.873	0.829	0.829
	I_p	0.172	0.220	0.183	0.152	0.195
	I_D	2.782	2.751	2.498	2.353	2.576
	I_w	1.775	1.623	1.636	1.669	1.628
	L/B	10.116	9.443	10.098	11.303	10.632
	S^*	1.155	1.363	1.246	1.241	1.461
	I_m	0.911	0.928	0.941	0.944	0.954

TABLE 7. Results of the parametric study when N is varied from 5 to 9. The other parameters are the same as in the reference case: $\mathrm{Re} = 10^5$, $\mathrm{AR} = 6$, $\mu_i = 10^4\,\mathrm{Pa\,s}$.

Appendix B. Variation of the aspect ratio

This Appendix addressed the influence of the aspect ratio AR on the characteristics and performances of the most efficient swimmers. As shown in figure 22, there is a slight advantage in having a lower aspect ratio, as the span of the tail increases in that case and the available thrust is larger too. But, the most important conclusion of this parametric study is that the main features of the Pareto front are conserved when aspect ratio is varied. In particular, the two main "species", the efficient swimmers and the fast swimmers, are recovered for all aspect ratios and their swimming gaits share common characteristics whatever the aspect ratio.

Examining the performances of the most efficient swimmers, it appears that their efficiencies E^* are also very similar (table 8), suggesting that aspect ratio is not a dominant effect here. There are two reasons for this. First, this is because the reduction of the
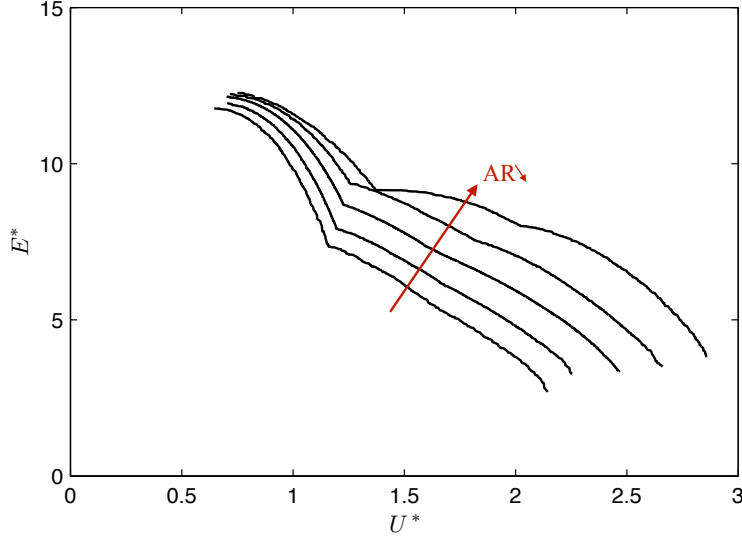
FIGURE 22. Results of the optimisation for different aspect ratios AR = 4, 5, 6, 7, and 8. The most efficient swimmers in each case are pictured in figure 23 and their characteristics are reported in table 8.
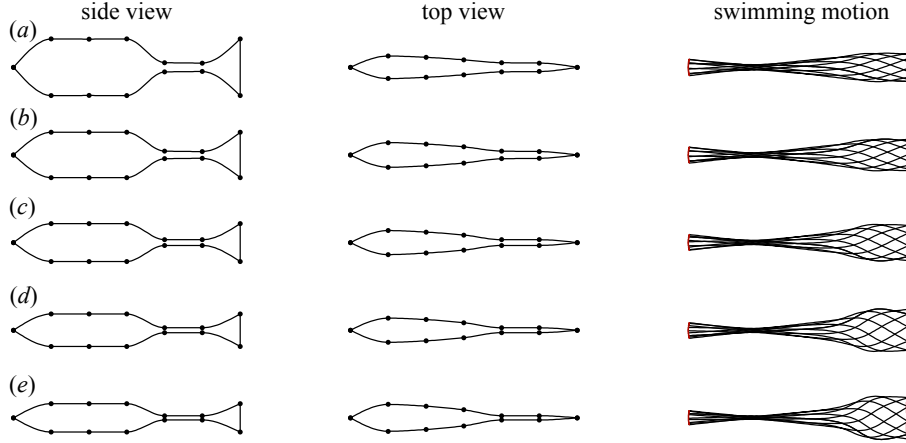

FIGURE 23. Geometry and kinematics of the most efficient swimmers when the aspect ratio is varied: (*a*) AR = 4; (*b*) AR = 5; (*c*) AR = 6; (*d*) AR = 7; (*e*) AR = 8. The characteristics and performances of these swimmers are reported in table 8.

tail span is accompanied by larger swimming amplitudes (the maximum incidence angle θ_{max} increases by more than 50% when aspect ratio is doubled as shown in table 8). And second, because the minimum allowed thickness is inversely proportional to AR, such that the swimmers with the largest aspect ratio are also the ones with the thinnest cross-section at the caudal peduncle. The internal dissipation is thus reduced for these swimmers, permitting larger curvature and hence larger amplitudes at a reduced cost.

The other observation that can be made by observing the dorsal views of the swimmers in figure 23 is that their maximum width B varies only slightly as the aspect ratio is modified. To explain this observation, one has to remember the conclusion reached above when the Reynolds number was varied: the volume of the anterior region is needed as an inertial 'flywheel' to prevent excessive pitching motions. In the present case, as the

Aspect ratio	AR	4	5	6	7	8
Figure		23a	23b	23c	23d	23e
Results	E^*	12.263	12.231	12.150	11.951	11.771
	U^*	0.751	0.716	0.702	0.705	0.646
	St	0.171	0.201	0.229	0.263	0.290
	Li	0.063	0.091	0.117	0.148	0.191
	$\theta_{\max}$	0.359	0.407	0.462	0.543	0.563
	U/V	0.670	0.647	0.632	0.628	0.599
	V_0	0.560	0.749	0.852	0.994	1.233
	I_p	0.208	0.228	0.220	0.215	0.240
	I_D	2.379	2.616	2.751	2.857	3.008
	I_w	1.514	1.558	1.623	1.669	1.644
	L/B	10.051	9.188	9.443	9.366	8.435
	S^*	1.166	1.242	1.363	1.422	1.454
	I_m	0.959	0.948	0.928	0.918	0.895

TABLE 8. Results of the parametric study when the aspect ratio AR is varied from 4 to 8. The other parameters are the same as in the reference case: $\mathrm{Re} = 10^5$, $N = 6$, $\mu_i = 10^4\,\mathrm{Pa\,s}$.

aspect ratio is reduced, so are the thrust and the torque produced by the reactive forces at the tail, and therefore the volume of the inertial anterior region does not have to be as large as in the case of small aspect ratios. For the present Reynolds number, it appears that the 'thickness aspect ratio' is approximately $L/B \approx 9$ for all aspect ratios.

Table 8 shows that E^* is a decreasing function of the aspect ratio. Therefore, if the optimisation calculations were performed without constraining the aspect ratio, one would expect small aspect ratio to be favoured, which is not compatible with the elongated-body assumption of the model.

Appendix C. Variation of the internal dissipation

Here, the dependence of the internal viscosity on the optimisation results is examined. It should first be noted that the value used for the reference case, i.e. $\mu_i = 10^4\,\mathrm{Pa\,s}$, has been chosen from the book of Schneck (1992) who reports measurements on isolated human muscle in the range $10^3 < \mu_i < 10^4\,\mathrm{Pa\,s}$. Approximately the same value, $\mu_i = 6 \times 10^3\,\mathrm{Pa\,s}$, has been used by Cheng *et al.* (1998) in their study of the internal mechanics of undulatory swimming, and more recently Tokić & Yue (2012) used $\mu_i = 10^4\,\mathrm{Pa\,s}$ in their optimisation model. To our knowledge, there has not been any direct measurement of μ_i on swimming animals, the only data being indirect, such as the study of Long *et al.* (2002), and thus hard to exploit in the present context.

In figure 24 are shown the results of the different optimisations as the internal viscosity is varied in the range $10^2 < \mu_i < 10^5\,\mathrm{Pa\,s}$. As expected, the swimmers with the lowest internal viscosities outperform the ones with higher viscosities, but the main features of the Pareto front are conserved. As μ_i is varied, the most efficient swimmers pictured in figure 25 exhibit a similar shape, the only difference being that the dorsal view is more streamlined as the viscosity is decreased, but maintaining an almost constant thickness such that $L/B \approx 9.5$. This is also evidenced in table 9 by observing that S^*, which measures the streamlining, is an increasing function of μ_i, whereas the volume V_0 and L/B are almost constant.

The swimming gaits of the different swimmers of figure 25 are also very similar, the only difference being that lower viscosities allow larger curvatures and thus largee amplitudes
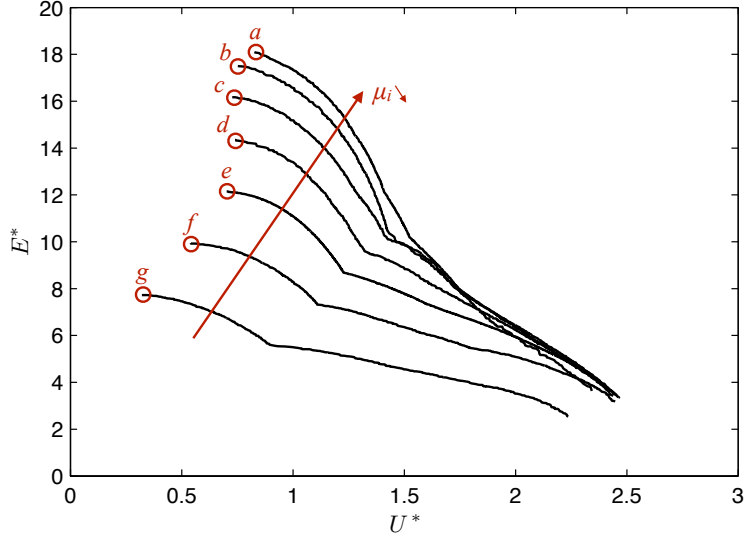
FIGURE 24. Results of the optimisation for different internal viscosities varying from $\mu_i = 10^2$ to 10^5 Pa s. The circles and the attached labels correspond to the most efficient swimmers in each case. These particular swimmers are pictured in figure 25 and their characteristics are reported in table 9.
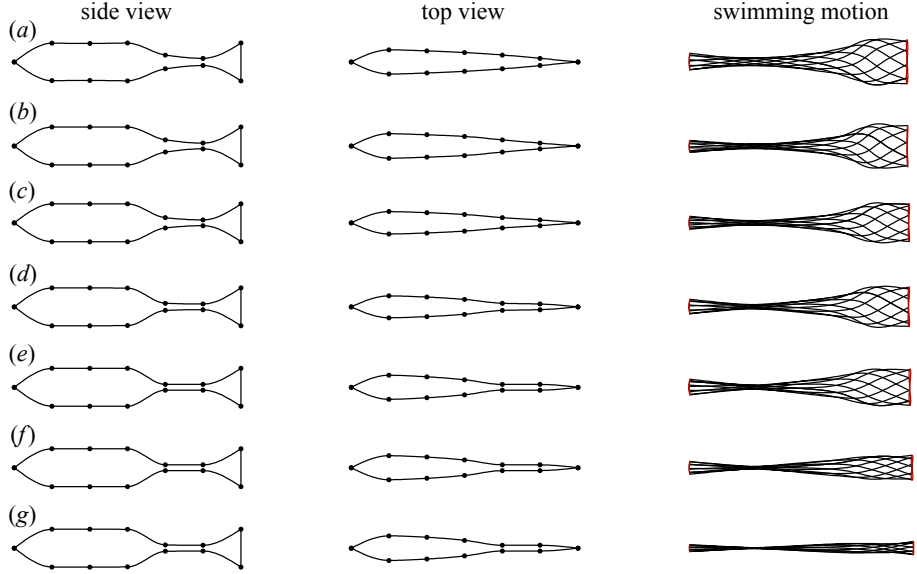

FIGURE 25. Geometry and kinematics of the most efficient swimmers when the internal viscosity is varied: (*a*) $\mu_i = 10^2$ Pa s; (*b*) $\mu_i = 3 \times 10^2$ Pa s; (*c*) $\mu_i = 10^3$ Pa s; (*d*) $\mu_i = 3 \times 10^3$ Pa s; (*e*) $\mu_i = 10^4$ Pa s; (*f*) $\mu_i = 3 \times 10^4$ Pa s; (*g*) $\mu_i = 10^5$ Pa s. The characteristics and performances of these swimmers are reported in table 9.

of the tail motion. Interestingly, this larger amplitude goes with larger stride length U^* such that the Strouhal number of the most efficient swimmers remains almost constant on the range $10^2 < \mu_i < 10^4$ Pa s (table 9). It should also be noted that for the smallest values of the internal viscosity, $\mu_i = 10^2$ Pa s (figure 25*a*), the anterior region of the swimmer is not perfectly rigid anymore but exhibits slight curvatures.

Viscosity	μ_i (Pa s)	10^2	3×10^2	10^3	3×10^3	10^4	3×10^4	10^5
Figure		25a	25b	25c	25d	25e	25f	25g
Results	E^*	18.095	17.498	16.174	14.344	12.150	9.950	7.724
	U^*	0.827	0.752	0.727	0.739	0.702	0.540	0.321
	St	0.235	0.244	0.230	0.237	0.229	0.204	0.185
	Li	0.110	0.113	0.107	0.109	0.117	0.119	0.120
	$\theta_{\max}$	0.493	0.513	0.480	0.501	0.462	0.353	0.213
	U/V	0.661	0.650	0.651	0.657	0.632	0.565	0.396
	V_0	0.987	0.979	0.872	0.808	0.852	0.861	0.879
	I_p	0.179	0.189	0.162	0.176	0.220	0.218	0.230
	I_D	2.356	2.436	2.425	2.561	2.751	2.777	2.788
	I_w	1.606	1.598	1.660	1.671	1.623	1.636	1.609
	L/B	9.349	9.261	10.142	10.363	9.443	9.440	9.211
	S^*	1.016	1.077	1.055	1.221	1.363	1.373	1.393
	I_m	0.947	0.952	0.938	0.938	0.928	0.927	0.958

TABLE 9. Results of the parametric study when internal viscosity is varied from $\mu_i = 10^2$ to 10^5 Pa s. The other parameters are the same as in the reference case: Re $= 10^5$, AR $= 6$, $N = 6$.

In the present study, it has been assumed that the internal viscosity, μ_i, remains constant as the Reynolds number is varied. This hypothesis makes sense if one thinks about this internal viscosity as an inherent property of the biological tissues. With this hypothesis, the 'internal Reynolds number' Re$_i$ constructed on μ_i scales as the Reynolds number Re, and consequently the relative importance of internal dissipation grows as Re is reduced. In other words, one expects, in that case, that small animals will be far more affected by internal dissipation and will corresponds to the largest viscosities studied here. An alternative hypothesis would be that the internal viscosity of the tissues varies with the animal size such that Re$_i$ remains roughly constant. This would mean that viscosity has been selected as a necessary mean for the controllability of the motion. This hypothesis should be testable by measuring internal viscosity on animals of different sizes. To this day, however, whether the former of the latter hypothesis applies remains a largely open question.

REFERENCES

ABRAMOWITZ, M. & STEGUN, I. A. 1965 *Handbook of Mathematical Functions*. Dover, New York.

ALEXANDER, R. M. 1977 Swimming. In *Mechanics and energetics of animal locomotion* (ed. R. M. Alexander & G. Goldspink), pp. 222–248. Chapman & Hall, London.

ANDERSON, E. J., MCGILLIS, W. R. & GROSENBAUGH, M. A. 2001 The boundary layer of swimming fish. *J. Exp. Biol.* **204**, 81–102.

BAINBRIDGE, R. 1958 The speed of swimming of fish as related to size and to the frequency and amplitude of the tail beat. *J. Exp. Biol.* **35**, 109–133.

BAINBRIDGE, R. 1963 Caudal fin and body movement in the propulsion of some fish. *J. Exp. Biol.* **40**, 23–56.

BLAKE, R. W. 1983 *Fish locomotion*. Cambridge Univ Press.

BLAKE, R. W. 2004 Fish functional design and swimming performance. *J. Fish Biol.* **65**, 1193–1222.

BORAZJANI, I. & SOTIROPOULOS, F. 2008 Numerical investigation of the hydrodynamics of carangiform swimming in the transitional and inertial flow regimes. *J. Exp. Biol.* **211**, 1541.

BRANKE, J., DEB, K., MIETTINEN, K. & SŁOWIŃSKI, R., ed. 2008 *Multiobjective optimization: interactive and evolutionary approaches*. Berlin: Springer.

CANDELIER, F., BOYER, F. & LEROYER, A. 2011 Three-dimensional extension of Lighthill's large-amplitude elongated-body theory of fish locomotion. *J. Fluid Mech.* **674**, 196–226.

CHENG, J.-Y., PEDLEY, T. J. & ALTRINGHAM, J. D. 1998 A continuous dynamic beam model for swiming fish. *Philos. Trans. R. Soc. Lond. B.* **353**, 981–997.

CHOPRA, M. G. & KAMBE, T. 1977 Hydromechanics of lunate-tail swimming propulsion. Part 2. *J. Fluid Mech.* **79**, 49–69.

CORNE, D. W., JERRAM, N. R., KNOWLES, J. D. & OATES, M. J. 2001 PESA-II: Region-based selection in evolutionary multiobjective optimization. In *Proceedings of the Genetic and Evolutionary Computation Conference (GECCO2001)*.

CURTIN, N. A. & WOLEDGE, R. C. 1993 Efficiency of energy conversion during sinusoidal movement of red muscle fibres from the dogfish Scyliorhinus canicula. *J. Exp. Biol.* **185**, 195–206.

D'AOÛT, K. & AERTS, P. 1999 A kinematic comparison of forward and backward swimming in the eel Anguilla anguilla. *J. Exp. Biol.* **202**, 1511–1521.

DODDS, P. S., ROTHMAN, D. H. & WEITZ, J. S. 2001 Re-examination of the "3/4–law" of metabolism. *J. Theor. Biol.* **209**, 9–27.

DONLEY, J. M. & DICKSON, K. A. 2000 Swimming kinematics of juvenile kawakawa tuna (Euthynnus affinis) and chub mackerel (Scomber japonicus). *J. Exp. Biol.* **203**, 3103–3116.

EHRENSTEIN, U. & ELOY, C. 2012 Skin friction on a moving wall and its implications for swimming animals. *J. Fluid Mech.* p. Submitted.

ELLERBY, D. J., SPIERTS, I. L. Y. & ALTRINGHAM, J. D. 2001 Slow muscle power output of yellow-and silver-phase european eels (Anguilla anguilla L.): changes in muscle performance prior to migration. *J. Exp. Biol.* **204**, 1369–1379.

ELOY, C. 2012 Optimal Strouhal number for swimming animals. *J. Fluids Struct.* **30**, 205–218.

ELOY, C., DOARÉ, O., DUCHEMIN, L. & SCHOUVEILER, L. 2010 A unified introduction to fluid mechanics of flying and swimming at high Reynolds number. *Exp. Mech.* **50**, 1361–1366.

ELOY, C. & SCHOUVEILER, L. 2011 Optimisation of two-dimensional undulatory swimming at high reynolds number. *Int. J. Nonlinear Mech.* **46**, 568–576.

FISH, F. E. & HUI, C. A. 1991 Dolphin swimming–a review. *Mammal Rev.* **21**, 181–195.

GILLIS, G. B. 1998 Environmental effects on undulatory locomotion in the American eel Anguilla rostrata: kinematics in water and on land. *J. Exp. Biol.* **201**, 949–961.

GRAY, J. 1933 Studies in animal locomotion. I. The movement of fish with special reference to the eel. *J. Exp. Biol.* **10**, 88–104.

GRAY, J. 1968 *Animal locomotion*. London: Weidenfeld & Nicolson.

HESS, F. & VIDELER, J. J. 1984 Fast continuous swimming of saithe (Pollachius virens): a dynamic analysis of bending moments and muscle power. *J. Exp. Biol.* **109**, 229–251.

HOERNER, S. F. 1965 *Fluid-dynamic drag*. Published by the author.

HOYT, J. W. 1975 Hydrodynamic drag reduction due to fish slimes. In *Swimming and flying in nature* (ed. T. Y.-T. Wu, C. J. Brokaw & C. Brennen), , vol. 2, pp. 653–672. Plenum, New York.

JAYNE, B. C. & LAUDER, G. V. 1995 Speed effects on midline kinematics during steady undulatory swimming of largemouth bass, Micropterus salmoides. *J. Exp. Biol.* **198**, 585–602.

KERN, S. & KOUMOUTSAKOS, P. 2006 Simulations of optimized anguilliform swimming. *J. Exp. Biol.* **209**, 4841–4857.

LAUDER, G. V. & TYTELL, E. D. 2005 Hydrodynamics of undulatory propulsion. *Fish Physiol.* **23**, 425–468.

LIGHTHILL, MJ 1969 Hydromechanics of aquatic animal propulsion. *Ann. Rev. Fluid Mech.* **1**, 413–446.

LIGHTHILL, M. J. 1960 Note on the swimming of slender fish. *J. Fluid Mech.* **9**, 305–317.

LIGHTHILL, M. J. 1970 Aquatic animal propulsion of high hydromechanical efficiency. *J. Fluid Mech.* **44**, 265–301.

LIGHTHILL, M. J. 1971 Large-amplitude elongated-body theory of fish locomotion. *Proc. R. Soc. Lond. B* **179**, 125–138.

LINDSEY, C. C. 1978 Form, function and locomotory habits in fish. In *Fish Physiology VII* (ed. W. S. Hoar & D. J. Randall), pp. 1–100. Academic Press.

LONG, J. H., KOOB-EMUNDS, M., SINWELL, B. & KOOB, T. J. 2002 The notochord of hagfish Myxine glutinosa: Visco-elastic properties and mechanical functions during steady swimming. *J. Exp. Biol.* **205**, 3819–3831.

OTA, T. & NISHIYAMA, H. 1984 Heat transfer and flow around an elliptic cylinder. *Int. J. Heat Mass Transfer* **27** (10), 1771–1779.

ROSEN, M. W. & CORNFORD, N. E. 1971 Fluid friction of fish slimes. *Nature* **234**, 49–51.

SCHLICHTING, H. 1979 *Boundary-layer theory*. McGraw-Hill, New York.

SCHNECK, D. J. 1992 *Mechanics of muscle*, 2nd edn. New York University Press.

TAYLOR, G. I. 1952 Analysis of the swimming of long and narrow animals. *Proc. R. Soc. London Ser. A* **214**, 158–183.

TOKIĆ, G & YUE, D. K. P. 2012 Optimal shape and motion of undulatory swimming organisms. *Proc. R. Soc. Lond. B* .

TRIANTAFYLLOU, G. S., TRIANTAFYLLOU, M. S. & GROSENBAUGH, M. A. 1993 Optimal thrust development in oscillating foils with application to fish propulsion. *J. Fluids Struct.* **7**, 205–224.

TRIANTAFYLLOU, M. S., TRIANTAFYLLOU, G. S. & YUE, D. K. P. 2000 Hydrodynamics of fishlike swimming. *Ann. Rev. Fluid Mech.* **32** (1), 33–53.

TUCKER, V.A. 1970 Energetic cost of locomotion in animals. *Comparative Biochemistry and Physiology* **34** (4), 841–846.

TYTELL, E. D., HSU, C. Y., WILLIAMS, T. L., COHEN, A. H. & FAUCI, L. J. 2010 Interactions between internal forces, body stiffness, and fluid environment in a neuromechanical model of lamprey swimming. *Proc. Nat. Acad. Sc. USA* **107**, 19832–19837.

TYTELL, E. D. & LAUDER, G. V. 2004 The hydrodynamics of eel swimming. I. Wake structure. *J. Exp. Biol.* **207**, 1825–1841.

VIDELER, J. J. 1993 *Fish swimming*, *Fish and fisheries Series*, vol. 10. London: Chapman & Hall.

WEBB, P. W., KOSTECKI, P. T. & DON STEVENS, E. 1984 The effect of size and swimming speed on locomotor kinematics of rainbow trout. *J. Exp. Biol.* **109**, 77–95.

WEIHS, D. 1973 Optimal fish cruising speed. *Nature (London)* **245**, 48–50.

WHITE, C. R. & SEYMOUR, R. S. 2005 Allometric scaling of mammalian metabolism. *J. Exp. Biol.* **208**, 1611–1619.

WU, T. Y. 2011 Fish swimming and bird/insect flight. *Ann. Rev. Fluid Mech.* **43**, 25.

WU, T. Y.-T. 1971a Hydromechanics of swimming propulsion. Part 2. Some optimum shape problems. *J. Fluid Mech.* **46** (03), 521–544.

WU, T. Y.-T. 1971b Hydromechanics of swimming propulsion. Part 3. Swimming and optimum movements of slender fish with side fins. *J. Fluid Mech.* **46** (03), 545–568.